Design of multi-junction solar cells on silicon substrates using a porous silicon compliant membrane

Matthew Wilkins

Thesis submitted to the Faculty of Graduate and Postdoctoral Studies in partial fulfillment of the requirements for the degree of

Master of Science

Systems Science Program
School of Electrical Engineering and Computer Science
University of Ottawa
Ottawa, Canada

Abstract

A novel approach to the design of multi-junction solar cells on silicon substrates for 1-sun applications is described. Models for device simulation including porous silicon layers are presented. A silicon bottom subcell is formed by diffusion of dopants into a silicon wafer. The top of the wafer is porosified to create a compliant layer, and a III-V buffer layer is then grown epitaxially, followed by middle and top subcells. Due to the resistivity of the porous material, these designs are best suited to high efficiency 1-sun applications. Numerical simulations of a multi-junction solar cell incorporating a porous silicon compliant membrane indicate an efficiency of 30.7% under AM1.5G, 1-sun for low threading dislocation densities (TDD), decreasing to 23.7% for a TDD of 10^7 cm^{-2}.

Statement of Originality

The author declares that he obtained the results presented in this thesis during the period of his M.Sc. research under the supervision of Dr. Karin Hinzer. This work is to the best of his knowledge original.

Certain aspects of the work described here were carried out by people other than the author. In particular, all solar cells and material samples were grown and fabricated by A. Boucherif, Artur Turala and others at CRN^2, Université de Sherbrooke. The experimental external quantum efficiency (EQE) of the G355 GaAs solar cell in Figure 14 was measured by Frédéric Asselin-Guay, and the methodology for simulating multi-junction solar cells as presented here is derived from earlier work by Gergö Létay and Martin Hermle of Fraunhofer ISE, and Alex Walker and Jeffrey F. Wheeldon of University of Ottawa.

The following contributions cover results presented in this thesis:

1. **M. Wilkins**, A. Boucherif, R. M. Beal, J. E. Haysom, J. F. Wheeldon, V. Aimez, R. Arès, T. J. Hall and K. Hinzer, "Multijunction Solar Cell Designs using Silicon Bottom Subcell and Porous Silicon Compliant Membrane", accepted for publication in *IEEE Journal of Photovoltaics*, revisions submitted Feb. 2013.
2. **M. Wilkins**, K. Hinzer, J. E. Haysom, R. M. Beal, A. Boucherif, V. Aimez and R. Arès, "Multijunction Solar Cell and Method for Forming the Same", United States provisional patent application number 61/760,360, filed Feb. 2013.

In addition, the following contributions are not directly related to the topic of this thesis, but are a result of research done during the period of the author's supervision with Dr. Hinzer:

3. **M. Wilkins**, A. Walker, J. F. Wheeldon, G. Arbez, H. Schriemer and K. Hinzer, "Design

Constraints of *p-i-n* GaAs/InGaAsN dilute Nitride Sub-cells for 3- and 4- Junction Solar Cell Applications under Concentrated Illumination", abstract submitted to 39th Photovoltaics Specialists Conference (Tampa FL, June 2013).

4. G. Arbez, A. Walker, **M. Wilkins**, J. F. Wheeldon, K. Hinzer and H. Schriemer, "4 Junction Dilute Nitride Solar Cell Optimization: Comparing Current Matching Approaches in Detailed Balance Algorithms", abstract submitted to 39th Photovoltaics Specialists Conference (Tampa FL, June 2013).
5. J. Mohammed, M. Yandt, **M. Wilkins**, A. Muron, T. J. Hall, J. E. Haysom, K. Hinzer and H. Schriemer, "Collection and Storage of Direct Spectral Irradiance and DNI Datasets with High Temporal Resolution for CPV Energy Yield Assessments", abstract submitted to 39th Photovoltaics Specialists Conference (Tampa FL, June 2013).
6. A. Walker, O. Thériault, **M. Wilkins**, J. F. Wheeldon and K. Hinzer, "Tunnel-junction-limited multi-junction solar cell performance over concentration", submitted to *IEEE Journal of Quantum Electronics* (Dec 2012).
7. **M. Wilkins**, R. Beal, J. E. Haysom, J. F. Wheeldon, P. Mulet, G. Jamieson, N. Youssef, D. Balachandreswaran, J. Fan, T. J. Hall, S. Myrskog and K. Hinzer (2011), "Design of a multiplexer to characterize individual optics at a concentrating photovoltaic test site". *Proc. SPIE 8007* (pp. 800725-800725-7). doi:10.1117/12.906246 (poster presented at Photonics North 2011, Ottawa, Canada)
8. R. M. Beal, **M. Wilkins**, J. F. Wheeldon, J. E. Haysom, C. E. Valdivia, M. Yandt, P. Dufour, *et al*. (2011), "Multi-kilowatt CPV Installation Employing Low-cost, Highly Concentrating Wave-Guiding Optics". Oral presentation at *7th International Conference on Concentrating Photovoltaic Systems: CPV-7* (pp. 239-242). Las Vegas, NV. doi:10.1063/1.3658335

9. G. Kolhatkar, **M. Wilkins**, A. Turala, B. Paquette, A. Boucherif, A. Jaouad, K. Hinzer, V. Aimez and R. Arès, "Effect of Te on the Performance of GaAs/GaAs Tunnel Junctions Grown by Chemical Beam Epitaxy For Photovoltaic Applications", poster presented at Next Generation Solar Photovoltaics Canada, 14-15 May 2012, Montreal, Canada
10. G. Kolhatkar, K. Hinzer, **M. Wilkins**, V. Aimez, R. Arès, A. Boucherif, A. Jaouad, B. Paquette, A. Turala, "Chemical Beam Epitaxy of Growth of GaAs/GaAs Tunnel Junctions for Multi-junction Solar Cells", poster presented at 8th International Conference on Photovoltaic systems (CPV-8), 16-18 April 2012, Toledo, Spain, P75
11. S. Schicho, **M. Wilkins**, A. Turala, A. Jaouad, A. Boucherif, A. Walker, J. F. Wheeldon, K. Hinzer, R. Arès and V. Aimez, "Effect of Ge Substrate Thinning on CPV Solar Cell Performance", poster presented at 8th International Conference on Photovoltaic systems (CPV-8), 16-18 April 2012, Toledo, Spain, P71
12. S. Schicho, **M. Wilkins**, A. Turala, A. Jaouad, A. Boucherif, A. Walker, J. F. Wheeldon, K. Hinzer, R. Arès and V. Aimez, "CPV solar cells with ultra thin Ge substrates", poster presented at Next Generation Solar, 14-15 May 2012, Montreal, Canada

Acknowledgements

First, a special thanks to my supervisor, Dr. Karin Hinzer, whose experience, guidance and enthusiasm are a great benefit to all of those in the SUNLAB research group. Thanks also to Dr. Henry Schriemer and the others in the group for great discussions and help over the past two years. Thanks to Dr. Abderraouf Boucherif, Dr. Artur Turala, Dr. Richard Arès, and Dr. Vincent Aimez of the Center for Research in Nanofabrication and Nanocharacterization (CRN^2) at Université de Sherbrooke for their work in supporting this project.

This research was performed at the SUNLAB research group, part of the Center for Research in Photonics at the University of Ottawa, from September 2011 to March 2013. Financial support was provided by Natural Sciences and Engineering Research Council (NSERC), Ontario Centres of Excellence (OCE), Canada Research Chairs Program, and Canadian Foundation for Innovation (CFI). Simulation tools and support were provided by CMC Microsystems.

Finally, I'd like to thank my friends and everyone in my family for their tremendous support and encouragement throughout my life.

Table of Contents

List of Figures

List of Abbreviations

CPV	Concentrating Photovoltaics
MOCVD	Metal-Organic Chemical Vapour Deposition
CBE	Chemical Beam Epitaxy
PV	Photovoltaic
ARC	Anti-Reflective Coating
CRN^2	Center for Research in Nanofabrication and Nanocharacterization at Université de Sherbrooke
XRD	X-Ray Diffraction
SEM	Scanning Electron Microscopy
FWHM	Full Width at Half Maximum
TDD	Threading Dislocation Density
STC	Standard Test Conditions
I-V	Current-voltage
V_{OC}	Open-circuit Voltage
I_{SC}	Short-circuit Current
J_{SC}	Short-circuit Current Density
EQE	External Quantum Efficiency
IQE	Internal Quantum Efficiency
SRH	Shockley-Read-Hall
TJ	Tunnel Junction
MJ	Multi-junction

1. Introduction

Since 2000, multi-junction solar cells designed for use under highly concentrated sunlight (i.e., concentration factors of 200 to 1000X) have shown the greatest gains in efficiency, as well as having the greatest absolute efficiency, of any solar cell technology [1]. Multi-junction solar cells also show the highest efficiency of any photovoltaic technology without concentration, however for economic reasons the use of such devices is typically limited to aerospace applications. In more cost-conscious applications such as terrestrial rooftop PV (photovoltaic) systems and larger PV farms, the market has always been dominated by single-junction silicon solar cells operating at 1-sun. This is in part because the silicon substrates used to make silicon solar cells are far less costly, and are available in larger sizes, compared with the germanium and GaAs substrates used in other designs.

Today, the cost of the solar cells is a fraction of the installed cost of a silicon-based, non-concentrating PV system. Other factors such as legal and administrative costs, labour and the 'balance of system' (parts of the system other than the PV modules) costs are also important components of the total system cost. If the cost metric for a particular PV technology is measured in dollars per watt-hour (i.e., cost of energy production), efforts to reduce the cost of silicon solar cells typically have small benefits since cell cost is already a small portion of the total system cost. In contrast, increases in cell efficiency have a much larger benefit since cell efficiency impacts the entire denominator in the cost/energy ratio. For this reason it is interesting to consider solar cell designs whose higher costs may be offset by efficiencies significantly higher than traditional silicon cells.

Currently, solar cells used in concentrating photovoltaic (CPV) systems are almost always multi-junction devices, with the most common configuration being a triple-junction design using a $Ga_{0.5}In_{0.5}P$ junction with 1.90 eV band gap, a GaAs junction with 1.42 eV band gap, and a germanium junction with 0.67 eV band gap. The cells are typically 5.5 mm by 5.5 mm in size and are grown epitaxially by metal-organic chemical vapour deposition (MOCVD) on a germanium substrate approximately 140 μm thick. A recent study showed that switching from a 100-mm-diameter (4") Ge to a 200-mm-diameter (8") Si substrate would result in a 60% decrease in the cost of multi-junction CPV solar cells [2, 3]. Current multi-junction cell designs are too costly for use without concentration, but if the cost can be sufficiently reduced, while maintaining high efficiency, it may be possible for multi-junction solar cells to be competitive with non-concentrating flat-plate PV systems.

Growing III-V materials with the lattice constant of GaAs on a silicon substrate is challenging due to the roughly 4% lattice mismatch between the crystal structures of silicon and the epitaxially grown materials. This work discusses one possible method of making a multi-junction solar cell on a silicon substrate using a porous silicon compliant membrane to accommodate the lattice mismatch. In order to do this, a silicon substrate would be prepared with a thin (~0.5 μm) top layer (a 'membrane') porosified using an electrochemical etching process. This porosified 'compliant substrate' would then be placed in a reactor for growth of III-V materials to form the GaAs and GaInP junctions. Epitaxial growth on porous silicon has been studied previously by Abderraouf Boucherif in his Ph.D work at Université de Lyon [4, 5], and more recently at Université de Sherbrooke, and the approach shows good potential for growth of lattice mismatched III-V materials [6]. The work described here focuses on numerical simulation of potential solar cell devices, informed by literature studies of the properties of the relevant materials, and by characterization of material samples grown and fabricated by collaborators at the Center for Research in Nanofabrication and Nanocharacterization (CRN^2) at Université de Sherbrooke.

This work stands in the context of similar work in the field. Growth of GaAs on silicon substrates has been studied by many researchers in the past, including some attempts using porous silicon compliant membranes [7–9]. Several groups have also studied methods of making multi-junction solar cells on silicon substrates. Perhaps the most successful of these methods, in terms of material quality and solar cell performance, has been the step-graded epitaxial growth of SiGe whose steadily increasing molar fraction of Ge eventually results in a lattice match with GaAs. Using this method, the Fitzgerald group at the Massachusetts Institute of Technology (MIT) [10] has demonstrated 16.8% efficiency under 1-sun AM1.5G conditions for a GaInP/GaAs dual-junction solar cell on a step-graded SiGe substrate, compared with 20.0% efficiency under the same conditions for a control cell grown on a GaAs substrate. Using this step-graded approach, Fitzgerald *et al*. [10] have been able to grow epitaxial layers of adequate quality, with threading dislocation densities of less than $10^6 \mathrm{cm}^{-2}$ that should yield good minority carrier lifetimes in the grown material. Threading dislocations and their relation to carrier lifetimes will be discussed further in section 3.3. The greatest disadvantage to this method is the thick (10 μm) layer of SiGe that is required; since growth of group IV and group III/V materials cannot generally be done in the same reactor due to contamination issues, two growth stages in different reactors are required. Additionally, due to its large thickness and small band gap, the step-graded SiGe buffer layer can be expected to absorb a large amount of light in the wavelength range that could be absorbed by a silicon bottom subcell, making a triple-junction GaInP/GaAs/Si design impractical.

Previously, researchers have also tried to form GaAs on silicon by wafer-bonding a thin

GaAs film to a silicon substrate, or by the use of a silicon-on-insulator (SOI) compliant membrane as an interface between the silicon and GaAs. These techniques are described in more detail in sections 2.2 and 2.3. The porous silicon compliant membranes studied here have not previously been examined for use in solar cells, and have potential for good performance while avoiding the high processing cost of the step-graded and wafer-bonded approaches, and the insulation between the substrate and epitaxial layers that is inherent in the SOI approach.

Researchers at Université de Sherbrooke led by Dr. Vincent Aimez are currently developing a process for growth of GaAs films in a porous silicon compliant membrane. While it is still unknown what quality of epitaxial material will finally be achieved using this technique, by studying possible designs for solar cells on porous silicon substrates we can estimate the performance that may be achievable given what is known about the porous silicon material, and we can determine the level of material quality that will be required in order to produce devices that are competitive with the state of the art.

The primary objective for this research is to identify an appropriate design for a multi-junction solar cell grown on a lower-cost silicon substrate, such as the one shown in Figure 1, using a thin porous silicon layer to accommodate lattice mismatch, and to estimate the expected efficiency using numerical simulations. An approach to the growth and fabrication of such a solar cell has been identified that is compatible with available techniques, based on the advice and expertise of the researchers at CRN^2. Methods for simulating multi-junction solar cell performance, previously developed by other researchers at SUNLAB, have been adapted to include layers of porous silicon within the multilayered heterostructure. Models of porous silicon band structure, carrier transport, and optical properties, as well as the impact of use of the porous silicon on the quality of the epitaxially grown layers, are included. Once the ability to simulate the performance of solar cells was developed, an optimization process was then used to adjust the available design parameters to maximize performance.

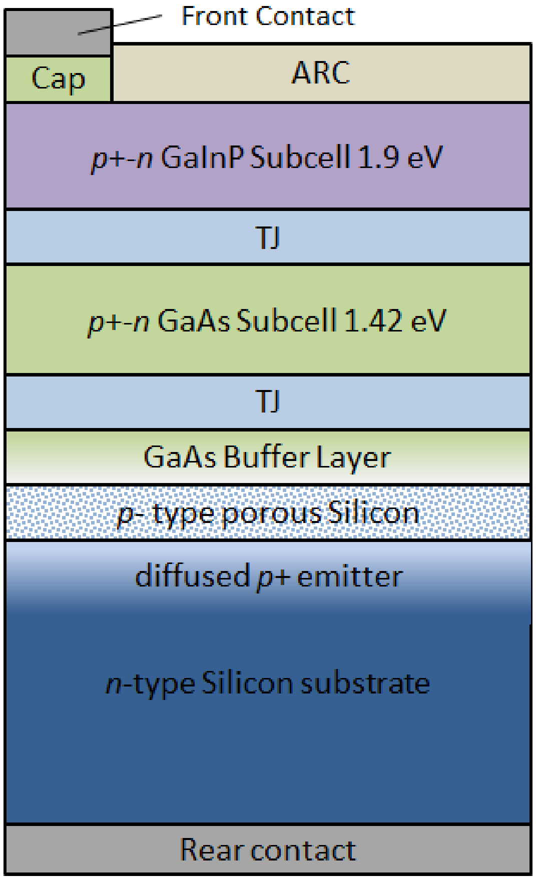

Figure 1: A possible structure for a triple-junction solar cell on a silicon substrate using a porous silicon compliant membrane.

In Chapter 2, background information on several relevant topics are presented, including the general properties of porous silicon, a review of literature on growth of GaAs on silicon substrates and current efforts to do so at Université de Sherbrooke, and general principles of solar cell design, including discussion of single- and multi-junction solar cells. Some common techniques for characterizing solar cells are introduced. In Chapter 3, the methodology of the present study is presented. The general method for numerical simulation of solar cells is described, and the standard test conditions used in this work are specified. Models for numerical simulation of devices including porous silicon layers are described in detail, and a method for modifying the properties of epitaxial layers to account for performance degradation due to dislocations is also included. Some of the design decisions involved in the choice of the cell design are addressed, along with the optimization of design parameters using a genetic optimization algorithm. Chapter 4 gives the final solar cell design that resulted from the optimization process, with the numerically simulated performance of the design for different levels of material quality. The resulting performance is compared with existing solar cell types, and factors limiting the performance are discussed. Chapter 5 presents conclusions of the research, with further discussion of the potential of this approach to making multi-junction solar cells and recommendations for further avenues of research. Finally, Appendix A provides an extensive list of material parameters that was compiled in preparation for this study. The list includes references to sources in the literature and some discussion in cases where there are multiple choices for values of a particular parameter.

2. Background

This project requires pulling together knowledge of semiconductor device physics and simulation, multi-junction solar cell design, fabrication and growth techniques, and properties of porous silicon. This chapter assumes a familiarity with the physics of semiconductor devices including single-junction solar cells, but some background detail in each of the areas listed above will be introduced in order to provide the reader with some context for the design study that is presented in the following chapters.

2.1. Porous Silicon

Porous silicon is formed by placing a regular silicon wafer in an electrochemical cell to etch pores in the surface. Depending on a variety of process parameters, the depth, morphology and size scale of the pores can be very accurately controlled. The material properties of porous silicon are reviewed by Canham [11], who points out that most properties are very highly dependent on the initial doping of the material, as well as the size and morphology of the porous structure. This work will focus primarily on porous silicon of 60% porosity, made from a *p*+ -doped layer of bulk silicon. These conditions generally result in an open-celled 'meso-porous' morphology. 'Meso' refers here to the approximate size range of the silicon crystallites, typically in the range of tens to hundreds of nanometers. This means that the crystallites are too large to cause quantum confinement of carriers, yet small enough to be treated as an effective medium from an optical point of view. Theiβ [12] has provided a thorough report on modeling optical properties of porous silicon using various forms of effective medium approximations.

The elastic modulus of an isotropic, open-celled porous material can be estimated as

$$Y = Y_0(1-p)^2 \tag{1}$$

where Y_0 is the elastic modulus of the bulk material and p is the volumetric porosity [13]. For porosities greater than 60%, the porous silicon will have an elastic modulus less than that of the silicon-on-insulator compliant substrates that are reviewed in section 2.2.

Meso-porous silicon generally has a band gap equal to that of bulk silicon [11]. This is different from nano-porous silicon, which often has significant quantum confinement and, as a result, a larger band gap. However, Si-H-B and Si-O-H bonds at the pore surfaces typically trap carriers that would otherwise be free to move within the silicon material [14], and these surface states create an electric field that further screens the interior of the silicon crystallites. As a result, porous silicon typically has many orders of magnitude fewer free carriers than the original bulk material. Timoshenko has done measurements on porous-Si/Si structures [14], and reported the results for 50% porous silicon made from a *p*+ doped silicon substrate. The details are given in section 3.2.3, where the numerical model for carrier transport in porous silicon is discussed.

In the context of optoelectronic devices, porous silicon has previously been studied for several possible applications. In light-emitting diodes (LEDs), experiments have been done with *nano*-porous silicon as the active material. The nano-scale structure of the material used in these devices results in quantum confinement that yields an increased bandgap and a suppression of the non-radiative Shockley-Read-Hall recombination mechanism (dominant in bulk silicon). At the same time, under Heisenberg's uncertainty principle, the spatial confinement of carriers implies a spreading of the carrier wavefunction in momentum space. This spreading can be sufficient to allow efficient recombination by a band-to-band transition, rather than the indirect transition that is required in bulk silicon [15]. Strong photoluminescence has been observed from this type of material, with an emission wavelength that can be tuned by varying the parameters of the porosification process to control the size of the silicon crystallites. The efficiency of actual LEDs has been limited, however, by the low conductivity of the nano-porous material. Sample LEDs typically show a very high series resistance and so require a large voltage bias to be applied.

Porous silicon has also been studied for use in silicon solar cells, as an anti-reflective material and/or as a material to passivate the front surface of the cell (in other words, to reduce surface recombination at the interface between the anti-reflective coating and the active silicon region).

2.2. GaAs Epitaxially Grown on Si Substrates

Several groups have studied the problem of epitaxial growth of GaAs on silicon substrates, and some have attempted to make multi-junction solar cells using a silicon substrate. Bolkhovityanov has provided an excellent review [16] of the state of the art in techniques for growth of GaAs on silicon, including methods involving some forms of compliant substrates (but not porous silicon compliant substrates specifically). Compliant substrates, where an interface material with low elastic modulus is placed between the substrate and epitaxial layers to accommodate changes in lattices constant, have yielded some of the highest quality epitaxial material, in terms of X-ray diffraction line width (XRD) of any of the current techniques. In particular, work by Pei *et al*. using a silicon-on-insulator (SOI) compliant substrate [17] yielded an estimated threading dislocation density of $3\mathrm{x}10^{7}$ cm^{-2}. SOI is not applicable for use in solar cells since it would not permit conduction between the top and bottom surfaces of the device, but values of elastic moduli similar to that of the SOI interface layer can be achieved with porous silicon of appropriate porosity and morphology. Studies of epitaxial growth on compliant membranes have shown that the presence of a layer with low elastic modulus produces an ‘image force’ acting on any dislocations in the epilayer, which tends to confine the dislocations to a region near the compliant membrane [17].

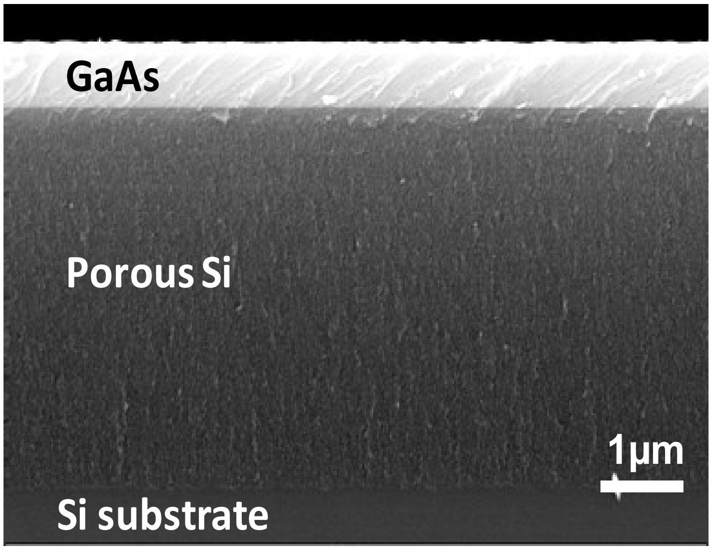

Figure 2: Scanning Electron Microscope (SEM) image of a GaAs film grown on a silicon substrate using a porous silicon compliant membrane. (from A. Boucherif, U. de Sherbrooke)

In addition to the problem of lattice mismatch, there are other potential difficulties with growth of GaAs on silicon, such as the formation of anti-phase domains, differences in thermal expansion coefficients, and the potential for incomplete bonds (and hence surface recombination centers) at the interface between group IV and group III/V materials.

The team of researchers at CRN^2, located at Université de Sherbrooke, have already done some initial growths of GaAs epi-layers on a porous silicon compliant substrate, with a focus on adjusting process parameters for optimal quality of the grown GaAs film. Figure 2 shows a scanning electron microscope (SEM) image of a cross-section of one of the grown samples. It can be seen that the GaAs forms a relatively uniform layer at this scale, however there are linear features in the GaAs layer which could be evidence of threading dislocations. Looking at the porous layer, it is evident that the scale of the pores is much less than 1 µm, which supports the assertion that the pores are much smaller than the optical wavelengths of interest and optical properties of the material can be modeled using an effective medium.

The quality of the GaAs in these samples can be evaluated in part by X-ray diffraction measurements, as shown in Figure 3. The full width at half maximum (FWHM) of the diffraction peak can be used to estimate an upper limit on the density of threading dislocations per unit area (TDD) in the crystal using the formula [18]

$$TDD \cong \frac{FWHM^2}{9b^2}, \tag{2}$$

where b is the Burgers vector representing the amount of distortion of the crystal lattice due to a single dislocation. In this case, we take b to be $a/\sqrt{2}$, where a is the crystal lattice constant [6], since this is consistent with the edge-type threading dislocations that are typically found in lattice

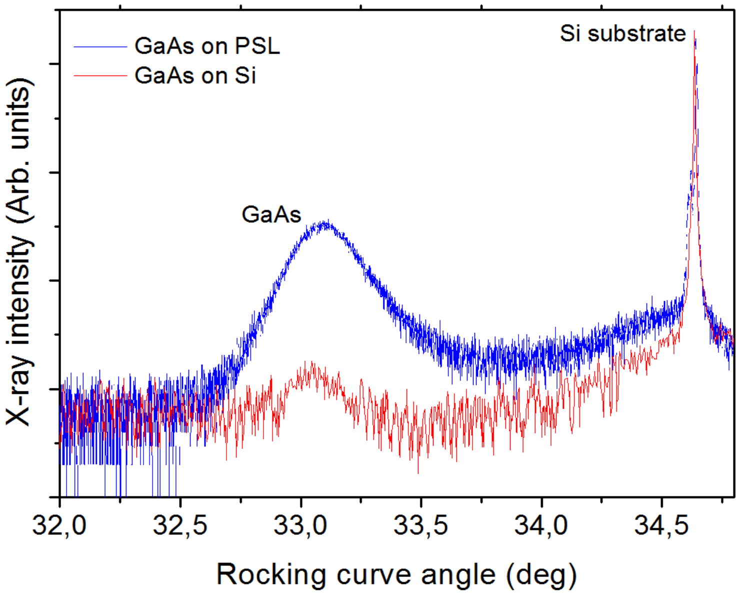

Figure 3: XRD rocking curve of a GaAs-on-porous silicon structure. The wide GaAs peak indiciates a high density of dislocations in the GaAs epilayer, which will result in low minority carrier lifetime. (From A. Boucherif, U. de Sherbrooke)

mismatched zincblende crystals. For the sample shown, the threading dislocation density is approximately 10^8 cm^{-2}. For reference, commercially available GaAs wafers typically have 10^4 – 10^5 threading dislocations per cm^2 [19]. Once the threading dislocation density is known, a minority carrier lifetime for recombination through defects associated with those dislocations will be [20]

$$\tau_{TDD} = \frac{4}{\pi^3 D \cdot TDD}, \tag{3}$$

where D is the diffusion coefficient for the carriers in question. Note that a second, perhaps more precise, method of evaluating TDD from XRD data is described in [21], although it was not used in this work. This method distinguishes between several factors that may contribute to the broadening of the diffraction peak, rather than attributing all of the broadening to dislocations. This technique is more involved since it requires additional XRD measurements with varying alignment of the sample, but it may be worth investigating in the future.

2.3. Single- and Multi-junction Solar Cells

An introduction to the operation of *p-n* junctions and photovoltaic cells is presented in J. Nelson's *The Physics of Solar Cells* [22], and in any semiconductor device textbook [23, 24]. Rather than explaining their operation from first principles, this section will illustrate certain concepts that are particularly relevant and also show some of the principles of good solar cell design.

Typical silicon and GaAs solar cell structures are illustrated in Figure 4. The cells are illuminated by photons incident on the top surface. The majority of photons are transmitted through the anti-reflective coating (ARC) and window layers, and photons of energy greater than the band gap of the active material are absorbed in the base and emitter regions to create electron-hole pairs. Since the absorption coefficients of the active materials generally increase with increasing photon energy, photons with energy significantly greater than the band gap have a high probability of being absorbed close to the top of the active region (the combination of the base and emitter layers) while lower energy photons will penetrate further before being absorbed. In order to ensure efficient absorption of incident photons, solar cells are generally designed with an active region thickness greater than the absorption length of the active material. Silicon solar cells have an active region hundreds of micrometers in thickness, while a GaAs cell, with its direct band gap, can absorb efficiently with only 1-2 μm of active region thickness.

The absorption of photons results in populations of minority carriers that are free to diffuse throughout the base and emitter regions. Once they reach the space charge region at the junction of the base and the emitter, the minority carriers will be swept across the junction by the built-in electric field, becoming majority carriers on the other side. Majority carriers can then be collected at the contacts to produce a photocurrent. In the absence of any recombination mechanisms, each absorbed photon will result in an electron contributing to the cell's photocurrent. In reality, recombination limits the diffusion length of the minority carriers. Carriers that are generated more than a diffusion length away from the space charge region have low probability of being collected and contributing to the photocurrent of the solar cell. Since diffusion lengths are typically much shorter in the highly-doped emitter layer than in the lower-doped base, solar cells are usually designed with a very thin emitter and a thicker base in order to allow carriers generated anywhere within the active region to diffuse efficiently to the space charge region.

Internal and external quantum efficiency (IQE and EQE) are important concepts to characterize the efficiency of optical absorption and carrier collection under short-circuit conditions. External quantum efficiency is the ratio of the number of electrons produced at the terminals of the solar cell to the number of photons of a particular wavelength incident on the cell. By sweeping the illuminating light source over a range of wavelengths λ, a plot of EQE as a function of wavelength can be produced. The cell's short-circuit current density (J_{SC}) is related to the EQE through

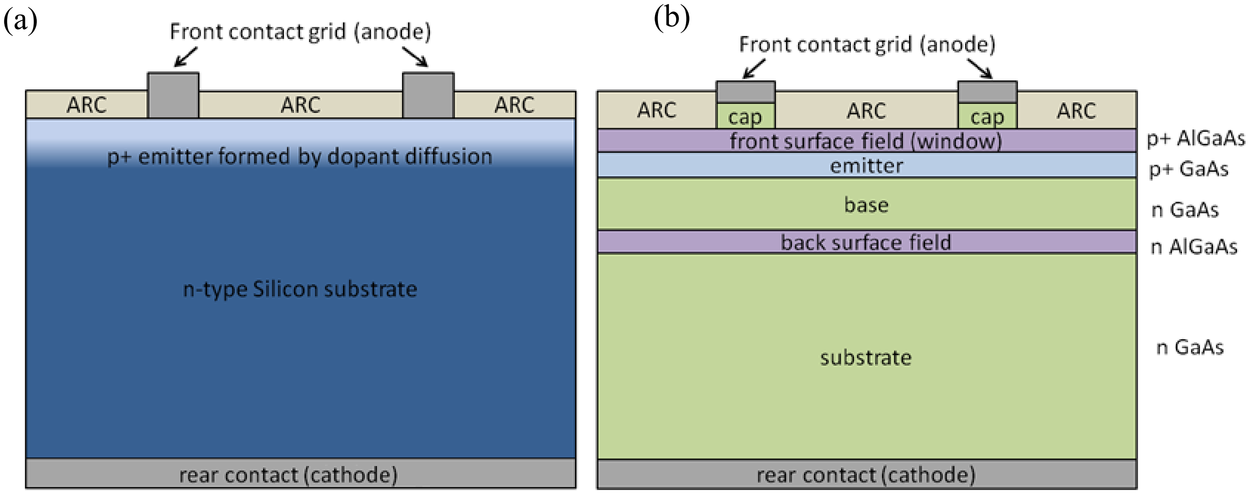

Figure 4: Structure of (a) a silicon solar cell and (b) a GaAs cell. Silicon cells are typically doped by diffusing dopant atoms into a wafer, whereas GaAs cells are grown epitaxially on top of a substrate. This enables the inclusion of additional material layers within the cell.

$$J_{SC} = \frac{q}{hc}\int_0^\infty \lambda \cdot EQE(\lambda) \cdot I(\lambda) d\lambda, \tag{4}$$

where q is the electron charge, h is Planck's constant, c is the speed of light and $I(\lambda)$ is the incident spectral irradiance. Whereas EQE is a measure of the efficiency of converting *incident* photons into carriers available at the device contacts, IQE measures the efficiency of converting *absorbed* photons into carriers. IQE is related to EQE through the expression

$$IQE(\lambda) = EQE(\lambda)/[1 - R(\lambda) - T(\lambda)], \tag{5}$$

where $R(\lambda)$ and $T(\lambda)$ are the spectral reflectance and transmittance of the device, respectively. In a plot of EQE as a function of wavelength, multiple phenomena are coupled, including reflectance due to index of refraction mismatch, recombination in the emitter, recombination in the base, gridline shading, and the absorption edge of the active material. IQE eliminates the dependence on reflectance and transmission, making it easier to isolate the effects of the remaining phenomena. It should be noted that the definitions of IQE and EQE used here apply to the macroscopic behaviour of a device, as is conventional in the context of solar cells. In other contexts, the term 'quantum efficiency' may be used in reference to the number of carriers generated locally per absorbed photon; in this case, the effect of recombination would not be included.

There are several recombination mechanisms present in any semiconductor device: radiative, Auger and Shockley-Read-Hall, which the primary mechanisms within the bulk material, and interface recombination is a form of Shockley-Read-Hall recombination that occurs at material interfaces. Under most conditions, the recombination rate for each mechanism, in each region, is dependent on the population of excess minority carriers in that region. As the bias on a cell increases from the short circuit toward the open-circuit condition, the excess minority carrier populations increase exponentially as a function of bias voltage. As a result, the recombination currents also increase exponentially with applied voltage, in typical diode fashion. In many cases one of these mechanisms, in one particular region of the device, is dominant and limits the open-circuit voltage (V_{OC}) of the entire cell.

Front surface fields (also called window layers) and back surface fields are usually added to epitaxially-grown solar cell designs. These layers serve to confine optically generated minority carriers within the region near the junction. They generally have a band gap greater than that of the active region, and are chosen to have a low value of interface recombination velocity between the active cell material and the material of the front or back surface field. Without front and back surface fields, photo-generated carriers would be free to diffuse far from the junction, where they could be lost to bulk recombination processes or recombination at surface states at an interface. The front and back surface fields prevent this outward diffusion and present interfaces with minimal surface states, reducing the both the bulk and surface recombination currents. This helps to achieve a high V_{OC} from the cell, and also improves J_{SC}.

Figure 5 illustrates the behaviour of a solar cell as the conditions change from (a) equilibrium, with no illumination and zero bias voltage, to (b) short circuit with illumination, to (c) open circuit with illumination. The device is a GaAs solar cell with *p*-*n* structure; light is incident from the left side of the diagram. The thin layer of high-bandgap material at $Y \sim 0.1$ µm is a GaInP front surface field, and the layer at $Y \sim 3.7$ µm is an AlGaAs back surface field. There is a *p*-doped, 1.0 µm thick emitter layer and a 2.6 µm thick *n*-doped base layer. At equilibrium (Figure 5a), the Fermi level (dashed line) is flat, indicating no net current flow anywhere in the device, and there is no separation between electron and hole quasi-Fermi levels. When the device is illuminated while maintaining a short circuit between contacts at the front and back of the cell, we have the short-circuit condition (Figure 5b). Light is absorbed within the active region, creating a population of minority carriers in the emitter and the base. In the emitter and the base, there is a gradient in the minority carrier quasi-Fermi levels (and hence in the minority carrier concentrations).

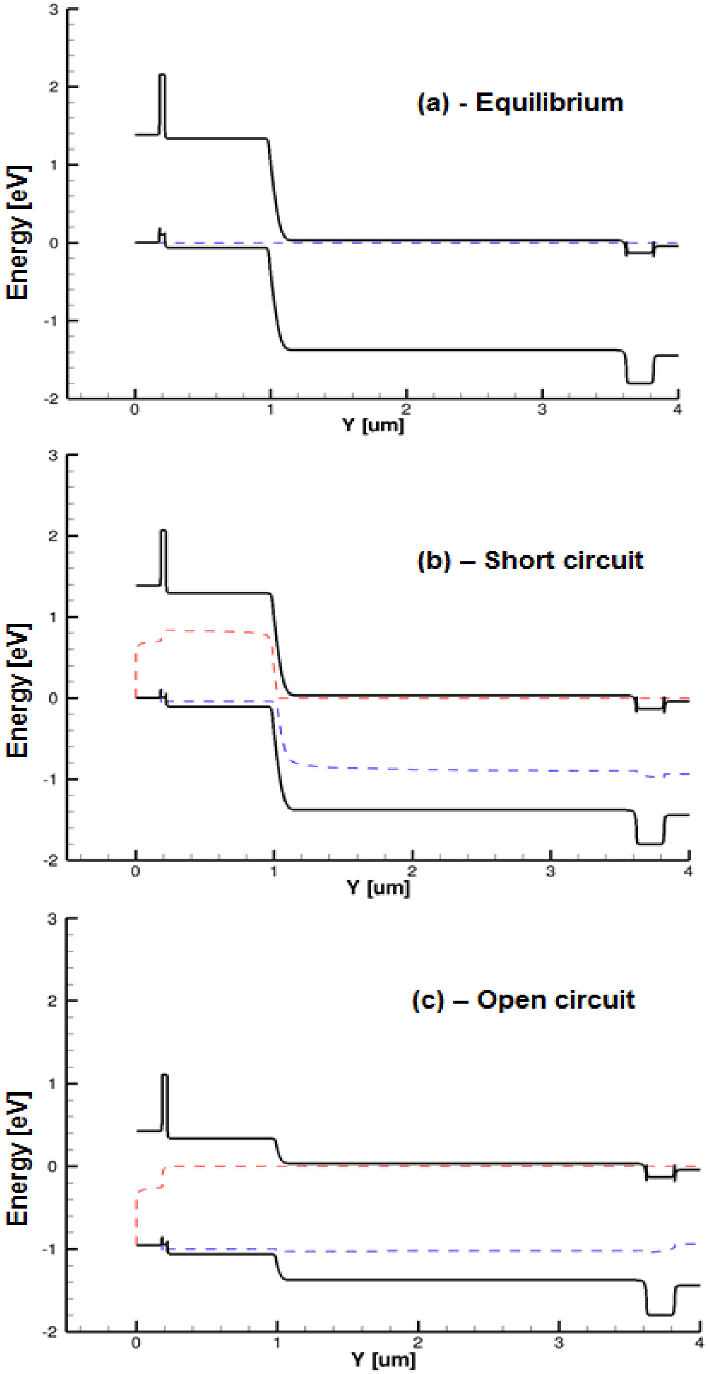

Figure 5: Numerically simulated band diagram of a GaAs solar cell with a *p-n* structure under equilibrium conditions (a), short circuit with 1-sun AM1.5D illumination (b), and open-circuit with 1-sun AM1.5D illumination (c). The black lines are the conduction and valence band energies; the dashed red lines are the electron quasi-fermi levels and the dashed blue lines are the hole quasi-fermi levels.

This gradient will cause minority carriers to diffuse towards the junction, where the electric field within the depletion region carries them across the junction and into the base (in the case of minority electrons) or into the emitter (in the case of minority holes). The front and back surface fields effectively prevent any diffusion away from the junction. With carriers steadily flowing in this way, a current can be collected at the device terminals.

When a positive bias is applied to the solar cell, it has the effect of offsetting the built-in voltage of the junction and reducing the band offset between the emitter and the base. At some value of bias, the width of the depletion region is reduced to the point that carriers are no longer carried across the depletion region and current is reduced to zero. This condition is open circuit (Figure 5c). With zero net current, the quasi-Fermi levels are again flat, and carrier concentrations are increased since they are not being removed through the external circuit.

A metallic grid is deposited on the top surface of solar cells to provide an electrical contact to the emitter side of the cell. The height and width of the gridlines must be optimized to provide minimal series resistance within the gridlines, while also minimizing the shading of the cell and the sheet resistance due to lateral conduction of carriers through the emitter to the contacts. This emitter sheet resistance can also be reduced by high doping of the emitter and increasing emitter thickness, but these also imply performance trade-offs.

A cap layer is typically added underneath the gridlines (see Figure 4b). This is a semiconductor layer specifically chosen to be of a material that will make good electrical contact with a metal. It may be a very highly doped thin layer of GaAs; by providing extremely high doping, any potential barrier at the semiconductor/metal interface should be thin enough that carriers can tunnel through it.

The cap layer is etched away everywhere except under the gridlines themselves, and an anti-reflective coating (ARC) is deposited everywhere else. This layer serves to minimize reflection of light at the interface between the semiconductor and the surrounding medium. Since front surface fields often contain aluminum, which is subject to oxidation when exposed to air, the ARC also serves the purpose of passivating the front surface field. The ARC may be fabricated from materials such as Si_3N_4, MgF_2, or TiO_2. A dual-layer combination of TiO_x and MgF_2 can make a very effective, broadband ARC and is often used in high-performance multi-junction cells.

Ideally, the perimeter of the solar cell should also be coated in a passivating material in order to seal the aluminum-containing layers where they intersect the edge of the cell, and to reduce surface recombination that occurs at the periphery of the cell. GaAs/air interfaces in particular have a very high surface recombination velocity.

Multi-junction solar cells are essentially a monolithic stack of *p*-*n* junctions (Figure 6). A large-band gap material (i.e., $Ga_{0.5}In_{0.5}P$) is used for the top junction, which absorbs photons from the highest energy portion of the spectrum, and provides a high V_{OC} with minimal thermalization losses. Light that is transmitted through the top subcell can then be absorbed by additional subcells (typically GaAs and germanium) below the GaInP subcell. At the interface between germanium (a group-IV material) and GaAs (a III-V compound), a GaAs nucleation layer is grown. This first layer of III-V material requires special attention to ensure that a high-quality zincblende lattice is initiated on top of the diamond lattice of the germanium.

The growth of the nucleation layer also has the effect of diffusing arsenic into the germanium, and most GaInP/GaAs/Ge cell designs take advantage of this diffusion to form the junction of the germanium subcell.The *p*-*n* junctions cannot be grown directly on top of one another, as electrons must be able to flow from the conduction band of one cell into the valence band of the next. Instead, tunnel junctions are created in between each pair of subcells. The tunnel junctions allow carriers to tunnel from the conduction band to the valence band with minimal voltage drop. When tunnel junctions are operating correctly, the tunnel junctions have roughly ohmic behaviour and have a negligible effect on the performance of the overall device.

Figure 7 shows a portion of the band diagram of a GaInP/GaAs/Ge muli-junction solar cell, including the GaInP subcell on the left and the GaAs subcell on the right. The two subcells are joined by a tunnel junction (an abrupt junction between a degenerately *n*-doped layer and a degenerately *p*-doped layer). When a small bias is applied to the tunnel junction, nonlocal band-to-band tunneling allows electrons to tunnel efficiently from the conduction band of the *n*-doped

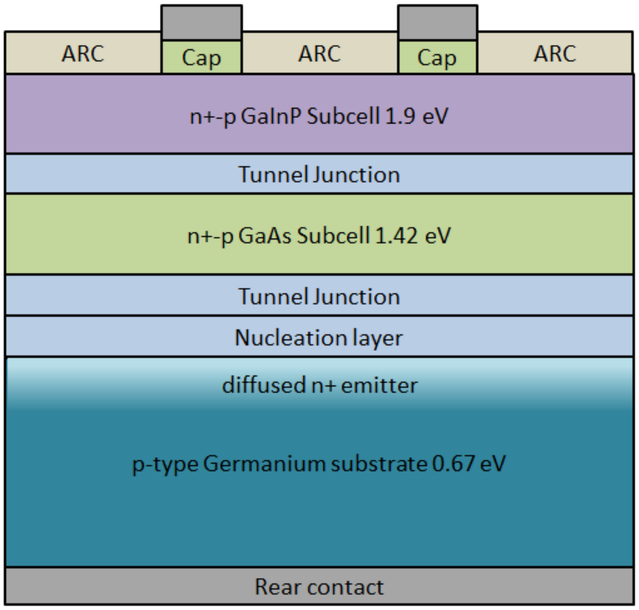

Figure 6: Simplified structure of a typical lattice-matched GaInP/GaAs/Ge multi-junction solar cell. The cell is grown epitaxially on a germanium wafer; the Ge junction is formed by diffusion of group-V atoms (typically phosphorous) from the nucleation layer.

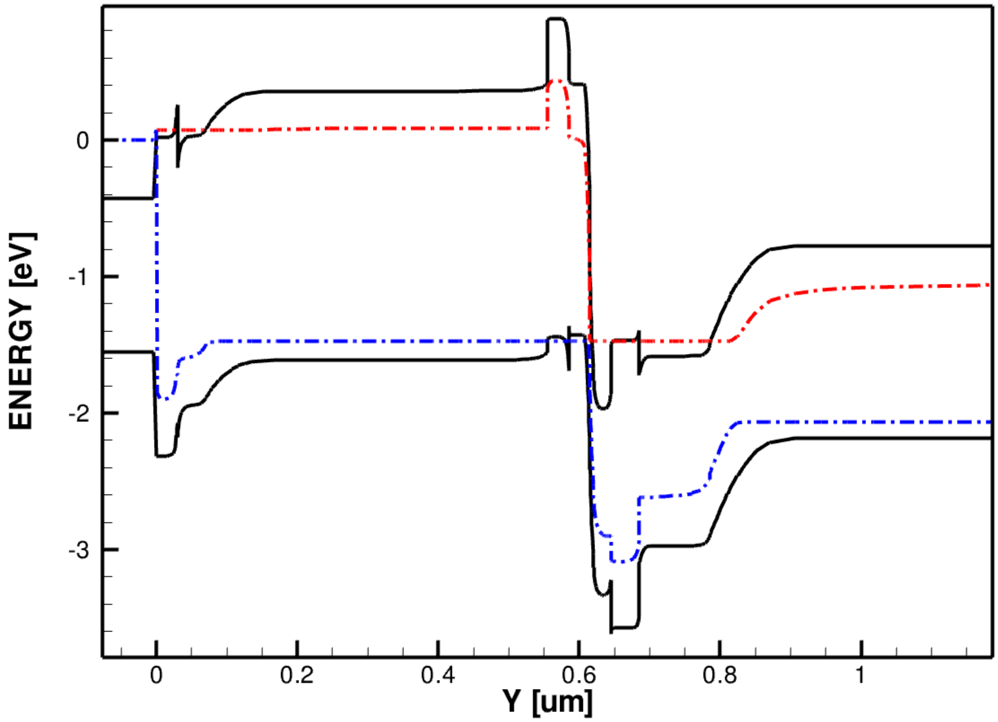

Figure 7: Energy band diagram of a multi-junction GaInP/GaAs/Ge solar cell, showing only the top (GaInP) subcell and a portion of the middle (GaAs) subcell. Between the two subcells, a tunnel junction consisting of an abrupt junction between a degenerately *n*-doped layer and a degenerately *p*-doped layer enables tunneling from the conduction band of one subcell into the valence band of the other.

layer on the right to the valence band of the *p*-doped layer on the left. This enables the flow of current from one sub-cell into the next. The use of tunnel junctions in multi-junction solar cells is discussed further in [25].

2.4. Solar Cells on Silicon Substrates

One of the most successful efforts to date for making multi-junction solar cells on silicon substrates has been the work by Fitzgerald *et al*. [10] at the Massachusetts Institute of Technology; they started with a silicon wafer and performed a step-graded growth of SiGe layers with gradually increasing germanium concentration, eventually reaching 100% germanium. This resulted in a ‘virtual’ germanium substrate with an approximate threading dislocation density of $1\text{x}10^6$ cm^{-2}. They then proceeded with the growth of a dual-junction GaInP/GaAs solar cell on the SiGe/Si substrate. While results were satisfactory for a first effort (19.8% efficiency compared with 23% for a control grown on a GaAs substrate), the process is unlikely to be of commercial interest since it requires several expensive processing steps, including epitaxial growth of approximately 10 μm of group-IV material, a chemical mechanical polishing step, and a consequent transfer into a second reactor for growth of III-V material.

As a part of their study, Fitzgerald *et al*. [20] studied single-junction GaAs solar cells grown on substrates of varying threading dislocation density. For high threading dislocation densities, the resulting reduction in minority carrier lifetime causes an increase in the solar cell’s dark current, and hence a decrease in open-circuit voltage (V_{oc}) and efficiency. If the dark current is described by the standard one-diode equation

$$J_{dark}(V) = J_0 e^{qV/nkT}, \qquad (6)$$

where J_0 is the diode saturation current density, q is the electronic charge, k is Boltzmann’s constant, n is the diode ideality factor and T is the temperature, the increased dark current manifests itself as an increase in J_0.

In single-junction GaAs solar cells, a threading dislocation density of $\sim10^6$ cm^{-2} or less is needed for good efficiency. Due to differences in diffusion lengths of n- and p-type GaAs, GaAs cells with a p-n structure tend to be more resilient to threading dislocations than are n-p structures.

At McMaster University, an alternative approach to producing multi-junction solar cells on silicon substrates uses wafer bonding [26]. In this approach, GaAs and GaInP subcells would be epitaxially grown on a GaAs wafer. After polishing the wafer surface to a high degree of flatness, the GaAs wafer would be bonded to a silicon wafer, and the III-V subcells would be etched away from the GaAs wafer using a selective etch. Like with the porous silicon approach, with this method it is challenging to produce a sufficiently low resistance silicon/GaAs interface.

3. Methodology

3.1. Numerical Modeling of Single- and Multi-junction Solar Cells

Within the SUNLAB research group at the University of Ottawa, numerical simulations of solar cells are done using a semiconductor simulation package from Synopsys Inc. called TCAD Sentaurus [27, 28]. Sentaurus is a composite suite of numerical programs used to simulate the performance of optoelectronics devices. It includes a solver that uses the finite difference method to compute a simultaneous solution to Poisson's equation, along with drift and diffusion equations on a meshed solution domain, from which the current-voltage characteristics of the device can be extracted. Additional effects can be added, such as optical transmission and generation, bulk recombination, tunneling, and others.

Solar cell models in Sentaurus represent a two-dimensional (2D) cross-section of a 'symmetry element' of the device. It includes half of a contact gridline and extends halfway to the next gridline. In this way, the model incorporates some 2D effects, such as sheet resistance and shading due to the top contacts, without the much larger mesh that would be required to represent a complete 2D or three-dimensional (3D) structure. On the other hand, this type of model does not include such effects as perimeter recombination, grid resistance losses and non-generation losses due to voltage drop across the top contact grid. It should be noted that these types can be modelled in Sentaurus with the user adding elements to the model. One approach to do this is outlined in [29]; this could be subject of future work. In studies of well-designed and fabricated solar cells, these effects are not normally significant and can be neglected without compromising the accuracy of the model. The current through the complete solar cell is calculated by multiplying the current through the minimal symmetry element by an 'area factor'.

Figure 8 gives an overview of the process for creating and running a device model. The first step is to specify the geometry of the various material regions and defining electrodes and boundary conditions. The domain is discretized, or 'meshed', at this point. Next, material properties are assigned to each material region. In preparation for this study, a literature review

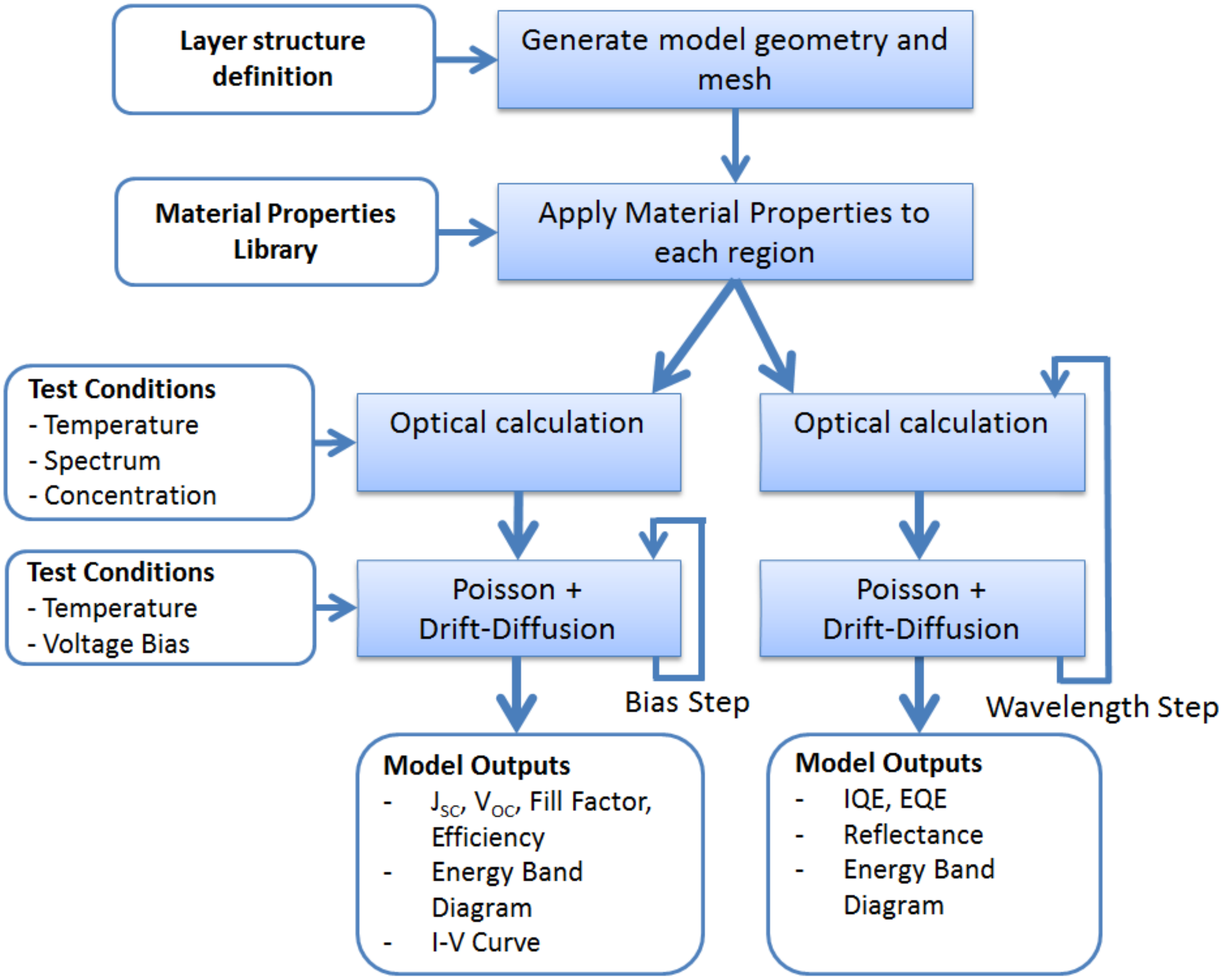

Figure 8: Process for generating and running a device model in Sentaurus. The left path is used to generate an I-V curve, and the right path is used to calculate EQE and IQE. This process is automated by Sentaurus Workbench, which runs each of the steps in sequence.

was done to determine the most appropriate properties to use for various materials; a listing of material properties used in this study is given in Appendix A. In order to calculate a solution under a particular illumination and bias condition, the solution proceeds in two steps. First, a transfer matrix method (TMM) is applied to calculate optical transmission and absorption within each layer of the solar cell, using a wavelength-dependent index of refraction and absorption coefficient for each material. This calculation can be done using a defined spectrum such as AM1.5G (to produce an *I-V* curve), or with a single wavelength at a time (to calculate quantum efficiency). For purposes of simulation, the incident light is generally assumed to be perpendicular to the cell, although this is not generally true in the case of flat-panel, fixed-tilt systems in actual operation, or in the case of CPV systems with high-concentration optics. Normal incidence is, however, the condition that is typically used in standard measurements of solar cell efficiency.

The TMM calculation outputs the absorbed optical power density as a function of position, which is converted into an optical generation rate, assuming 100% efficiency in the conversion of absorbed photons into carriers. This generation rate is used as an input to the main equation solver, where the Poisson and carrier transport equations are solved. The top contact grid shades a portion of the cell, and so the optical generation is only applied to the un-shaded area of the cell. Diffraction at the edges of the gridlines is not taken into account; however this is not expected to cause any error in the total optical power absorbed by the cell. Shockley-Read-Hall, radiative, Auger, and surface recombination mechanisms are also included at this point, and a lumped series resistance representing the gridline resistance is added at the anode. To calculate an *I-V* curve, the equations are solved repeatedly as the bias on the contact electrodes is swept over a range of voltage. In the case of the quantum efficiency, the contacts are maintained at short circuit and the wavelength of incident light is swept over the appropriate range, with the TMM solution being recalculated at each step.

3.1.1. Differential Equations in the Bulk Regions

The electrical potential and carrier concentrations in semiconductor materials are calculated using three coupled differential equations, as outlined in the Sentaurus Device User's Guide. Poisson's equation relates the electrical potential to charge distributions within the solution domain as [27, p. 185]

$$\nabla \cdot \varepsilon \nabla \phi = -q(p - n + N_D - N_A) - \rho_{trap}, \tag{7}$$

where ε is the dielectric constant, ϕ is the electrical potential, q is the electronic charge, p and n are hole and electron concentrations, N_D and N_A are donor and acceptor concentrations, and ρ_{trap} is the density of fixed charges in trap states. For this work, no trap states are defined and so ρ_{trap} is set to zero.

The electron and hole continuity equations are formulated as [27, p. 191]

$$\nabla \cdot \vec{J}_n = qR_{net}(n,p) + q\frac{dn}{dt} \tag{8}$$

and

$$-\nabla \cdot \vec{J}_p = qR_{net}(n,p) + q\frac{dp}{dt}\ , \tag{9}$$

where $\vec{J}_n$ and $\vec{J}_p$ are the electron and hole current densities, respectively, and $R_{net}(n,p)$ is the net recombination rate (the sum of all optical generation and recombination processes) and is a function of the carrier concentrations. For studies of the operation of solar cells, we are only interested in steady-state solutions, so the time derivatives of n and p will be zero. Using the drift-diffusion model for current transport and applying the Einstein relation, the electron and hole current densities may then be written as [27, p. 193]

$$\vec{J}_n = -nq\mu_n \nabla E_{F,n} \quad (10)$$

and

$$\vec{J}_p = -pq\mu_p \nabla E_{F,p} \ , \quad (11)$$

where μ_n and $\mu_p$are the electron and hole mobilities and $E_{F,n}$ and $E_{F,p}$are the electron and hole quasi-Fermi levels. Relating the conduction band energy and valence band energy E_C and E_V to the material properties and the electrostatic potential, we have [27, p. 187]

$$E_C = -\chi - q(\phi - \phi_{ref}) \quad (12)$$

and

$$E_V = -\chi - E_{g,eff} - q(\phi - \phi_{ref}) \ , \quad (13)$$

where χ is the electron affinity of the material, $E_{g,eff}$ is the effective band gap (including the effect of band gap narrowing), and ϕ_{ref} is an arbitrarily chosen reference potential.

Using Fermi-Dirac statistics for the electron and hole concentrations and making the assumptions that the carrier populations and the crystal are at a constant temperature throughout the device and that the conduction and valence bands have parabolic band structures, the electron and hole quasi-Fermi levels are [27, p. 188]

$$E_{F,n} = kT\mathcal{F}_{1/2}^{-1}\left(\frac{n}{N_C}\right) + E_C \quad (14)$$

and

$$E_{F,p} = -kT\mathcal{F}_{1/2}^{-1}\left(\frac{p}{N_V}\right) + E_V \ , \quad (15)$$

where k is Boltzmann’s constant, T is the device temperature, $\mathcal{F}_{1/2}^{-1}$ is the inverse Fermi-Dirac integral of order 1/2, and N_C and N_V are the effective densities of states in the conduction and valence bands, respectively. By substituting (10), (12) and (14) into (8) and substituting (11), (13) and (15) into (9), we arrive at a formulation of the three coupled differential equations for steady state problems, stated solely in terms of the material properties and functions of the three variables n, p and ϕ:

$$\nabla \cdot \varepsilon \nabla \phi = -q(p - n + N_D - N_A)\ , \tag{16}$$

$$\nabla \cdot \left[n\mu_n \nabla \left(kT\mathcal{F}_{\frac{1}{2}}^{-1}\left(\frac{n}{N_C}\right) - \chi - q\left(\phi - \phi_{ref}\right) \right) \right] = -R_{net}(n,p)\ , \tag{17}$$

and $$\nabla \cdot \left[p\mu_p \nabla \left(kT\mathcal{F}_{\frac{1}{2}}^{-1}\left(\frac{p}{N_V}\right) + \chi + E_{g,eff} + q\left(\phi - \phi_{ref}\right) \right) \right] = -R_{net}(n,p). \tag{18}$$

The solution of the coupled differential equations follows the method of Bank and Rose [30, 31]. Formulation of the equations and considerations for achieving robust and stable solutions of the equations, as well as discretization are discussed in these two papers.

A complete discussion of the recombination-generation term would be beyond the scope of this thesis, however it is a sum of generation and recombination rates at each point within the domain [27, p. 349]:

$$R_{net}(n,p) = R_{SRH}(n,p) + R_{Auger}(n,p) + R_{Rad}(n,p) - G. \tag{19}$$

The optical generation rate *G* is the result of the TMM calculation that is performed prior to solving the coupled differential equations (16-18), with the assumption that each absorbed photon results in a generated carrier. The recombination rates R_{SRH}, R_{Auger}, and R_{Rad} are calculated from the electron and hole carrier populations according to models for the Shockley-Read-Hall [27, p.349], Auger [27, p. 366] and radiative [27, p. 365] recombination processes respectively. In the tunnel junctions, where band-to-band tunneling is considered, there is no longer a single quantity R_{net} to describe generation/recombination in the valence band and in the conduction bands. Instead, the two bands are treated separately.

3.1.2. Discretization: The Box Method

Sentaurus device uses the Box Discretization Method [32] to approximate the continuous differential equations (16-18) as a set of linear difference equations, each representing a small area of the solution domain. Figure 9 illustrates a small portion of the solution domain for a simulation of a GaInP solar cell. The domain has been divided into a mesh of triangular elements.

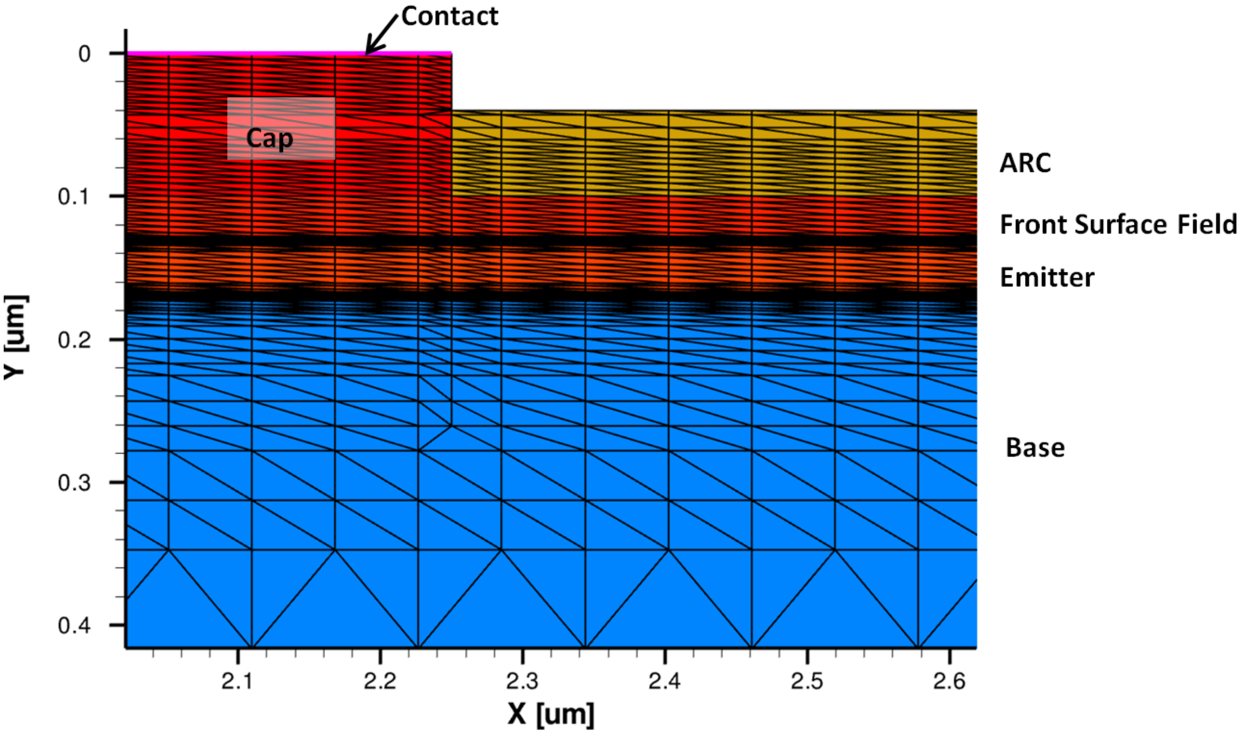

Figure 9: A portion of the mesh for a GaInP solar cell. The complete solution domain measures 60 um in the x axis by 600 um in the y axis. Mesh density is refined near the region interfaces, where gradients in the solution are greatest.

In the box discretization method, a 'Voronoï Box' is constructed around each mesh vertex (Figure 10) by bisecting each of the edges leading away from the vertex. Using Gauss' theorem, each of the continuous differential equations (16-18) are then transformed from the form [27, p. 935]

$$\nabla \cdot \vec{J} + R = 0 \tag{20}$$

into difference equations of the form

$$\sum_{j \neq i} d_{AB} \cdot j_{ij} + \mu(\Omega_i) \cdot r_i = 0 \ , \tag{21}$$

where d_{AB} is the distance between points A and B, j_{ij} is the linear flux density across the interface between box Ω_i and the adjoining box Ω_j, $\mu(\Omega_i)$ is the area of box i, and r_i is the sink/source rate per unit area. The summation is performed over each of the edges of box Ω_i.

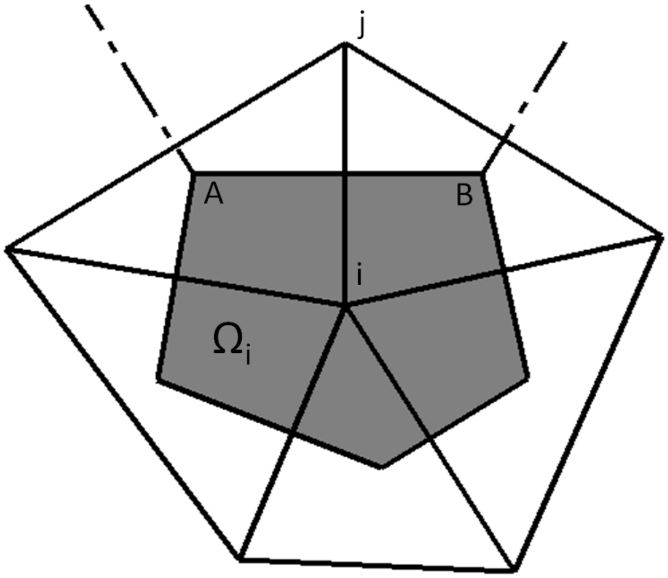

Figure 10: A Voronoï Box Ω_i is constructed by bisecting the mesh edges originating from vertex i. Gauss' theorem is used to relate fluxes across the edges of the Voronoï box to sink or source terms within the area of the box. The dashed lines represent edges of the box for vertex j.

3.1.3. External Boundary Conditions

At all external boundaries of the solution domain where no electrical contacts are defined, a Neumann boundary condition is applied, meaning that the components of any fluxes normal to the boundaries are zero:

$$\left.\begin{aligned} &\vec{\nabla}\phi \cdot \hat{n} = 0, \\ &\vec{J}_n \cdot \hat{n} = 0, \\ \text{and} \qquad &\vec{J}_p \cdot \hat{n} = 0. \end{aligned}\right\} \tag{22}$$

These boundary conditions specify that no current flows across the external surfaces of the domain. This is applicable both to the top surface of the cell, and also to the periodic boundary conditions at the lateral edges of the domain. The structure is effectively 'mirrored' at the periodic boundaries, so it follows that normal gradients must be zero there in order to have a continuous solution across the periodic structure.

Where ohmic contacts are defined at an interface, the boundary conditions are instead defined by assuming that the electron and hole concentrations are at equilibrium adjacent to the contact:

$$n = n_0 \ \text{ and } \ p = p_0. \tag{23}$$

This stands to reason as the quasi-Fermi levels are continuous across the semiconductor-metal interface, since the carrier population in the metal itself is always at equilibrium.

3.1.4. Internal Boundary Conditions: Heterojunctions

Multi-junction solar cells are heterostructures, meaning that they contain abrupt junctions of different materials and hence abrupt steps in conduction and valence band energies, effective intrinsic carrier concentrations, and other properties. Since the bulk equations for carrier transport (16-18) include the gradients of these quantities, they are not applicable at the heterojunction interfaces. Instead, the interfaces are treated by splitting the solution domain into separate regions for each different material and then specifying an internal boundary condition to define the transport of carriers across the interfaces between regions.

The physics of transport across an interface is based on the theory in [33], and application to numerical simulation is outlined in [34], which Sentaurus has adapted for the use of Fermi-Dirac carrier distributions. Under some circumstances, junctions between very highly doped layers of different materials form very sharp, narrow barriers in the conduction or valence bands, and so it is possible to have tunneling through these barriers. Sentaurus' treatment of heterointerfaces includes both thermionic emission 'over the barrier' and tunneling through the barrier. Although the model includes some empirical parameters that are not necessarily known for all material combinations, any resulting error is expected to be small for typical multi-junction solar cell designs since transport across these interfaces is not normally a limiting factor in performance. However, for a heterojunction solar cell (such as a CdS/CIGS cell) where the diode behaviour is defined by transport across the heterojunction, calibration of the thermionic emission parameters could be very important.

3.1.5. Standard Test Conditions

Solar cells that are being evaluated for use in flat-panel systems (without concentration) are normally tested under 'standard test conditions' (STC) which are defined as an AM1.5G spectrum [35] with an intensity of 1000 W/m^2, at a cell temperature of 25°C. Illumination is incident normal to the cell surface. These same test conditions are used for simulations in Sentaurus.

3.1.6. Validation of Solar Cell Modeling Capability

The ultimate goal of this work is to use numerical simulation to evaluate the potential performance of a multi-junction solar cell on a silicon substrate using a porous silicon compliant membrane. Since the quality of the results of any simulation is dependent on the input parameters, the project must begin with an extensive literature study for each of the materials in question. This is now complete and a report with recommended baseline model parameters and has been shared with others working on device simulation at SUNLAB [36], reproduced in Appendix A. The report covers material parameters for the five main active materials used in crystalline solar cells: GaAs, GaInP, germanium and silicon. For each material it includes the necessary parameters for band structure, doping-dependent mobility, radiative, Auger and SRH recombination process, and profiles of optical absorption and index of refraction, with references to the original sources. It also includes reported surface recombination velocities for a variety of material interfaces.

Despite the effort to use the most appropriate physical models available and to use the most up-to-date parameters, there are still a number of assumptions within the modeling approach that cannot be directly confirmed from first principles or by reference to the literature. For example, the assumption of parabolic band structure in equations (13) and (14) does not necessarily hold at very high doping levels, and the parameters for the thermionic emission model are not known for all material combinations. In general, errors in these parameters are not expected to significantly impact the overall results of a simulation, however further validation of the modeling technique is required to demonstrate this. This further validation was carried out by comparing the measured performance (current-voltage characteristics and external quantum efficiencies) of four custom-grown GaAs single-junction solar cells, of a known structure, with a model generated in Sentaurus. The solar cells were grown and fabricated at CRN^2 (Université de Sherbrooke), and so the exercise also provided an opportunity to become familiar with the CRN^2 team's cell growth capabilities. The cell design was a *p*-*n* structure, with no anti-reflective coating (ARC) and no back surface field (Figure 11).

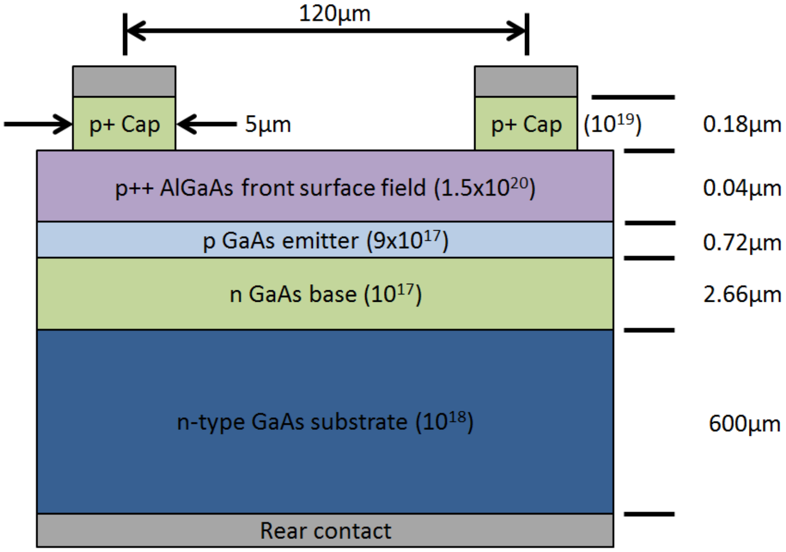

Figure 11: Layer structure of the GaAs single-junction solar cell used for validation of the Sentaurus modelling capability. Doping levels in cm^{-3} are given in parentheses.

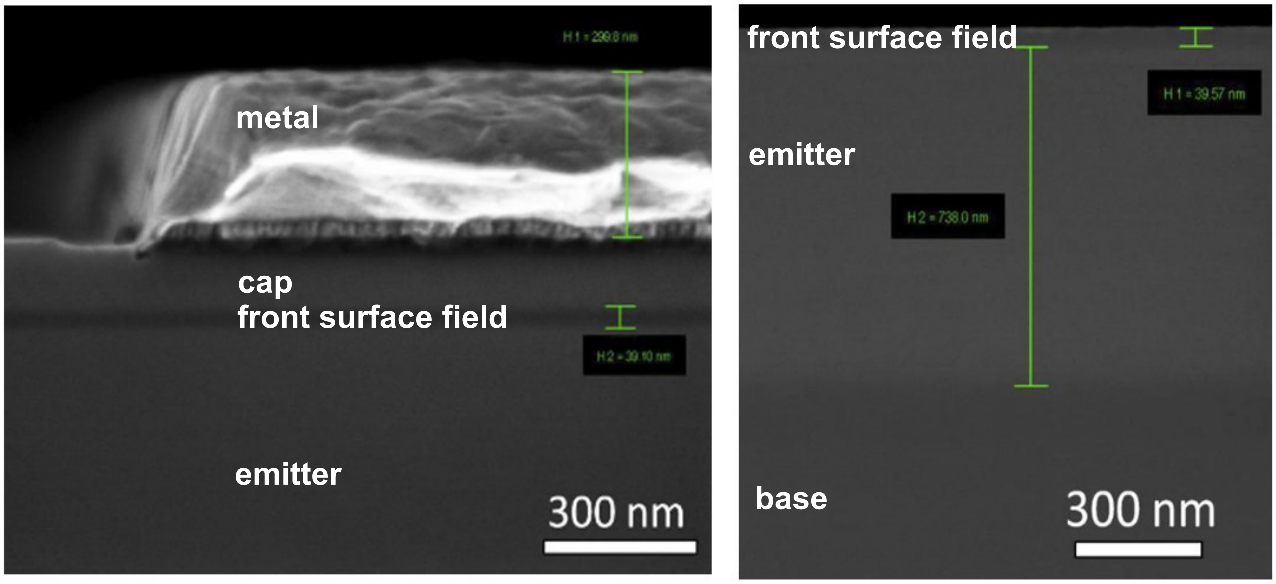

Figure 12: Cross-sectional SEM images of the G355 run of GaAs single-junction solar cells, showing layer thicknesses. (Left) top of cell and gridline, prior to etching away the cap layer. (Right) front surface field and emitter, after etching of the cap layer. Images provided by A. Boucherif, Université de Sherbrooke.

Due to issues of uncontrolled carbon doping of aluminum-containing layers, the front surface field layer was doped to an extremely high concentration of $1.5\text{x}10^{20}/\text{cm}^3$, which could cause a poor band alignment between the emitter and the front surface field, as well as causing high surface recombination at the emitter/front surface field interface. The relatively simple structure of this cell design, combined with knowledge of the layer thicknesses measured directly from SEM images (Figure 12), was very beneficial when comparing measured cell performance against simulations as there were very few unknown quantities in the fabricated devices. The four cells made in this way were labeled G355A, G355B, G355C and G355D.

Current-Voltage (*I-V*) measurements were taken on the four cells using a Keithley 2601A source/measure unit with a 4-probe connection to the solar cell, both under dark (non-illuminated) conditions and with an Oriel model 92191-1000 solar simulator approximating an AM1.5D spectrum. As was described in section 2.3, the dark *I-V* characteristic is predominantly a result of recombination processes in the active region of the solar cell, and so comparing the dark *I-V* measurements with simulations can help to fine-tune recombination parameters in the simulation. The measured data is plotted in Figure 13, with the current plotted on a log scale on the vertical axis. The measured data was fitted to the formula, derived from a two-diode model [22, p. 163],

$$J_{dark} = J_0\left(e^{\frac{q(V-J_{dark}R_{series})}{n_0 kT}} - 1\right) + J_1\left(e^{\frac{q(V-J_{dark}R_{series})}{n_1 kT}} - 1\right), \tag{24}$$

with the following fitted parameters:

J_0	7x10^{-10} A
n_0	2.2
J_1	7x10^{-20} A
n_1	1.0
R_{series}	0.09 Ω

The two-diode model allows us to account for two different diode-type processes operating in parallel with different values of ideality factor. In fact, it is generally expected that radiative and Auger processes, as well as SRH processes occurring outside the depletion region of the solar cell, show a diode behaviour with an ideality factor of 1. The SRH process occurring inside the depletion region, where the populations of both electrons and holes are of comparable magnitude, has an ideality factor of roughly 2 [22, p. 164]. By plotting current on a log scale (Figure 13), the exponential terms appear as straight lines and it becomes easier to distinguish the regions of operation where the dark current is dominated by a process of ideality factor 1 or of ideality factor ~2. Below 0.9V, the dark *I-V* characteristic is dominated by diode behaviour with ideality factor 2.2. Between 0.9 and 1.05V, a slight upward bend in the *I-V* curve is noticeable on careful inspection, and at the highest bias, above 1.0V, there is a curvature due to series resistance of the solar cell. The upward bend can be reproduced with the second diode curve of ideality factor 1.0. Although this is only a very minor feature of the *I-V* curve, the ability to estimate the magnitude of this second current component is extremely useful, as it provides information on the relative importance of different recombination processes that are present within the cell. In a different GaAs cell design, this second component could be much more prominent.

When the solar cell structure was reproduced in Sentaurus, it was not possible to exactly recreate the ideality factor 2.2 portion of the dark *I-V* curve. The SRH mechanism in Sentaurus results in an ideality factor of 2.0, which gives a noticeably different slope in the plot of

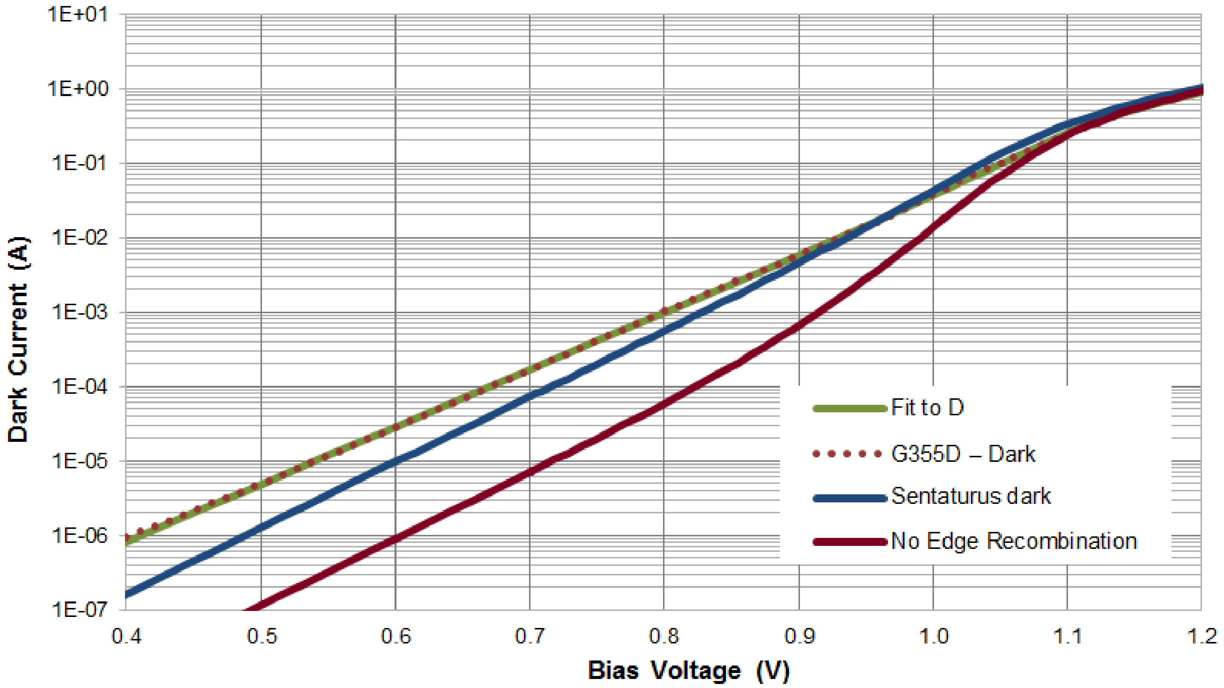

Figure 13: Measured dark current of the G355D solar cell (dotted), with a fit to the 2-diode model (green), as well as results of Sentaurus simulations with and without recombination at the perimeter of the cell (blue and red respectively).

log(current) vs. voltage in the region below 0.9 V, between the measured and simulated curves. It was not possible to match the magnitude of the $n = 2.2$ current (i.e., match the measured value of J_1) without also increasing the $n = 1.0$ current to greater than what was measured.

In the end, the only way to roughly match the measured *I-V* characteristic to the simulation was to introduce surface recombination at the perimeter faces of the solar cell. Since no passivation was applied to the cell edges, the GaAs/air interface could conceivably have a surface recombination velocity on the order of 10^6 cm/s. Since the plane of the cell's depletion region intersects with these faces, we can expect that there will be a significant contribution to the $n \sim 2$ component of the dark current due to this surface recombination. Unfortunately, the usual simulation approach of modeling only a reduced portion of the solar cell does not necessarily represent perimeter recombination very well, as the lateral distance that carriers must travel to reach the perimeter is underrepresented.

To evaluate the importance of this shortcoming, a few experimental simulations were done using a half-symmetry 2D model representing half of the full width of a solar cell, exploiting the fact that the lateral boundary conditions are equally applicable to device edges or to planes of symmetry. In order to simplify the geometry, the entire top surface of this model was covered in a contact rather than making thin gridlines as in a normal cell; this should not have a large effect on the cell behaviour under dark conditions. This 'half-symmetry' model showed similar results to the usual reduced symmetry model, if the surface recombination velocity at the perimeter of the reduced symmetry model was adjusted by a factor of w_{grid}/w_{cell}, where w_{grid} is the spacing between gridlines and w_{cell} is the width total of a cell. This factor scales the perimeter recombination current to account for the fact that the reduced 2D model has more perimeter

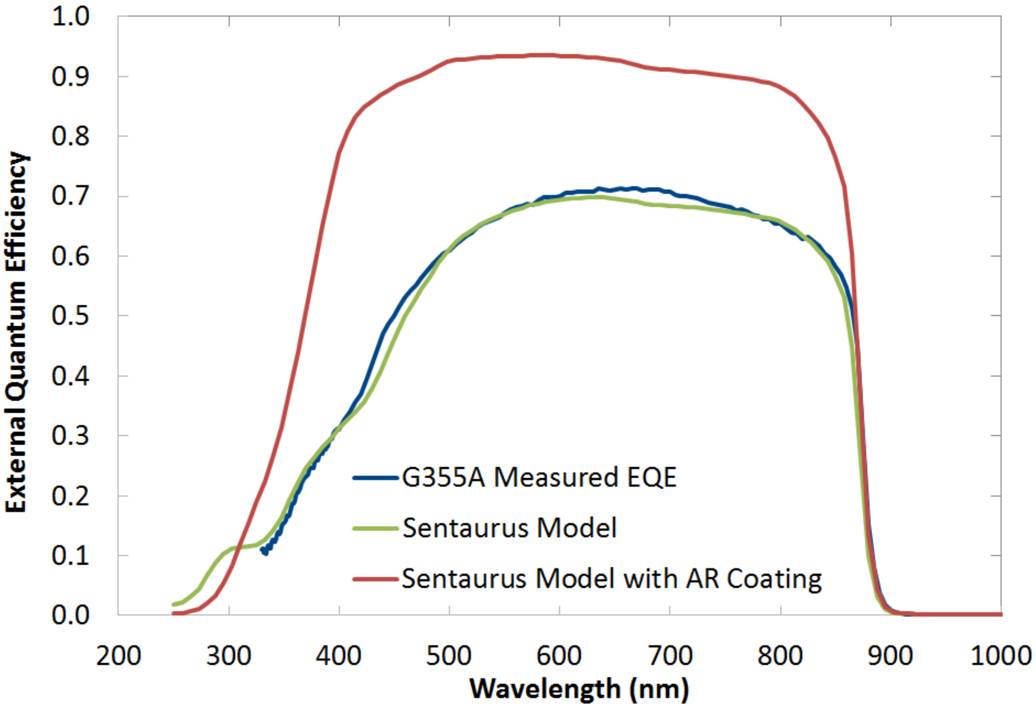

Figure 14: External quantum efficiency (EQE) of single-junction GaAs solar cell G355A. By adjusting a few material parameters such as electron and hole lifetimes in GaAs, it was possible to acheive a close fit to the measured EQE data.

surface area in relation to the top surface area, compared with the actual solar cell.

With perimeter recombination included in this way, it was possible to produce a higher $n = 2$ current in the simulation without increasing the $n = 1$ current excessively, and so a better fit to the measured data was possible. This result, shown in blue in Figure 13, was the best possible match to the measured dark *I*-*V* data. This introduces some error in the calculated efficiency, as will be discussed below.

The external quantum efficiency (EQE) of the cells was also measured (Figure 14) and compared against the Sentaurus model. The ‘shoulders’ of the EQE curve at 500 and 900 nm are influenced by minority carrier lifetimes in the emitter and base: shorter lifetimes result in more rounded shoulders. A good fit to the EQE curve then indicates that the minority lifetime values in the model are approximately correct.

The simulated EQE is also very sensitive to the optical absorption profiles of the active material and of the front surface field layer. While it may appear that the peak EQE is quite low at approximately 70%, it must be noted that the cell did not include an anti-reflection coating. As an experiment, in Sentaurus a typical broadband 2-layer TiO_x/MgF_2 anti-reflective (AR) coating was applied to the top surface of the cell, and this showed an increase to a peak EQE of ~93% and a much squarer shoulder at short wavelengths – indicating that the rounded shoulder there was a result of reflectivity losses from the air-semiconductor interface, and not a deficiency in carrier collection. As a result, the short-circuit current (I_{SC}) of the cell with anti-reflective coating is expected to be improved.

Table 1 gives a summary of the measured current density-voltage (*J-V*) curve parameters of the four G355 series GaAs solar cells, along with the results of Sentaurus simulations with and without an anti-reflective coating. *J-V* curve metrics of two high-performance GaAs solar cells reported in the literature [22, p. 195, 37] are also provided for comparison. Note that current density is defined here as the cell current divided by the cell's 'designated area', which includes the area covered by gridlines, but excludes any area covered by busbars [38].

There is a good match in the measured and simulated short-circuit current density (J_{SC}), as might be expected since J_{SC} is closely related to the cell's EQE and a good match of the EQE was shown in Figure 14. It should be noted, though, that there may be some error in the measured J_{SC} values, because a correction was not made for the difference between the spectrum of the solar simulator and the reference AM1.5G spectrum used in the simulations. This is because, at the time of the measurements, no spectrometer was available to measure the solar

Table 1: *J-V* curve metrics for the G355 single-junction GaAs solar cells, compared with Sentaurus simulations. Also included are two 'champion' GaAs solar cells reported in the literature. J_{SC} values for the G355 measurements may have some significant error as no correction was made for the spectral mismatch between the solar simulator and the AM1.5G spectrum that was used for the data in the other columns.

	Fraunhofer GaAs cell	**Kopin GaAs Cell**	**Sentaurus with ARC**	**Sentaurus no ARC**	**Cell G355A**	**Cell G355B**	**Cell G355C**	**Cell G355D**	**G355 Average**
V_{OC} (V)	1.038	1.022	0.983	0.968	0.956	0.957	0.959	0.962	0.958
J_{SC} (mA/cm^2)	29.7	28.2	31.4	22.0	21.3	20.8	20.8	21.2	21.0
Fill Factor, %	84.7	87.1	81.6	81.2	77.1	74.1	72.8	76.8	75.2
Efficiency, %	26.1+/- 0.8	25.1	25.2	17.3	14.0	13.1	13.2	15.0	13.9

simulator's spectrum. Also, the adjustment of the lamp intensity was done to a precision of, at best, +/-0.5% due to variations in the lamp intensity over time. This uncertainty causes a corresponding uncertainty if +/- 0.5% in J_{SC} and in efficiency. As a result, a comparison of the measured and simulated EQE is more meaningful than a comparison of the measured and simulated J_{SC}.

The fill factor (*FF*) is defined as

$$FF = \frac{V_{mp}J_{mp}}{V_{OC}J_{SC}} , \qquad (25)$$

where V_{mp} and J_{mp} are the voltage and current at the maximum-power point of the cell's *J-V* curve, respectively. The fill factor reported by the simulation (81.2%) is greater than the average value measured from the G355 cells (75.2%), or in fact any one of the individual G333 cells. In cells where parasitic resistances do not have a strong effect, the fill factor is closely related to the ideality factor of the *p-n* junction, with a higher ideality factor producing a less 'square' *I-V* curve and a lower fill factor. As was shown in Figure 13, the cell's dark current at a bias near the cell's V_{OC} (~0.95V) is dominated by a process with ideality factor n = 2.2, whereas in the simulation a process with $n = 1$ is dominant at a bias of 0.95V.

The performance metrics of V_{OC}, J_{SC}, and fill factor combine to give the cell's efficiency,

$$\eta = \frac{V_{OC} J_{SC} FF}{E} \ , \tag{26}$$

where E is the intensity of light incident on the cell (1000 W/m^2 under standard test conditions). The average efficiency of the four cell samples was 13.9%, while the efficiency produced by the Sentaurus simulation was 17.3%. The discrepancy is mainly due to the difference in fill factor, and is related to the perimeter recombination which is present at the un-passivated cell edges and which has a voltage dependence that cannot be accurately represented in the reduced 2D Sentaurus model.

Passivating the perimeter faces of the solar cells would likely have reduced the $n = 2.2$ recombination process and improved the fit between the simulation and the measurement. Indeed, commercially produced multi-junction solar cells typically have their perimeter passivated, and so perimeter recombination is not normally a strong influence on performance. In the future, it would be advisable to also passivate the perimeters of test samples, in order to prevent this effect from dominating a sample's performance and obscuring other components of the dark current which are of interest.

Despite the discrepancy in fill factor and the resulting difference in simulated vs. measured efficiencies, the simulation successfully reproduced the EQE of the GaAs cell using material properties taken from the literature and a cell structure derived from measured layer thicknesses of the actual structure. The EQE calculation is done under short-circuit conditions, and so it does not include the effect of the voltage dependence of the device. The values of V_{OC} also showed better agreement once perimeter recombination was introduced at the edge of the solution domain. Based on these results, it seems that the modeling approach presented here has good predictive capability when applied to epitaxially grown solar cells of this type, especially in cases where perimeter passivation is minimized through a passivating coating.

In any numerical simulation study, it is important to study convergence of the solution with respect to discretization in order to ensure that the discretization error is acceptable. The modeling approach used here was originally developed and validated by Gergö Létay of Fraunhofer ISE, and convergence studies are reported in [39]. Létay also performed sensitivity studies on a number of design and material parameters and evaluated their influence on J_{SC}, V_{OC}, fill factor, efficiency and EQE. Similar mesh densities were used in this work, and additional convergence studies were done to confirm those results and in areas where the model was significantly modified from the one developed by Létay. In particular, the bottom subcell is much thicker in this work, and so extra care was taken in discretizing those layers.

3.2. Models of Porous Silicon Properties

Compared with other modeling work done previously at SUNLAB, the most novel part of this project is the modeling of the carrier transport in the porous silicon layer and the interfaces between it and the bulk layers above and below it. In order to include the porous layer in the model without explicitly modeling the microstructure of the pores, it must be represented as an ‘effective medium’, i.e., a bulk layer of material whose properties are representative of the microstructured material.

In the structures considered here, porous silicon is only used for conduction of majority carriers; it is not used for purposes of generation or transport of minority carriers, and so minority carrier lifetime should not be critical to the accuracy of the model. Properties that are very significant include majority carrier concentration, mobility, band gap, index of refraction and to some extent, absorption coefficient. Models and/or values for each of these parameters were found from a reading of the literature, and are presented below.

3.2.1. Optical properties

Index of refraction is important because, if there are large differences in indices of refraction, the interface between the porous silicon material and the surrounding layers could form a reflective interface that would prevent light from reaching the bottom silicon subcell. The absorption properties are also important, but it is expected that any generated carriers will recombine without being collected by the silicon subcell. Theiβ did an extensive study of optical properties of porous silicon layers for a variety of compositions [12]. For meso-porous silicon of moderate (< 70%) porosities, it seems that the Looyenga effective medium approximation [40] is the best available model that does not require specific calibration against measured samples. It relates the effective dielectric function of the porous material to the dielectric functions of the bulk material and the material filling the pores. The Looyenga approximation, which is derived from a theoretical model involving a mixture of dielectric materials, uses the formula

$$\varepsilon_{eff}^{1/3} = p\varepsilon_{air}^{1/3} + (1-p)\varepsilon_{bulk}^{1/3} \ , \tag{27}$$

where ε_{eff} is the effective dielectric function of the porous material, ε_{air} is the dielectric function of the air filling the pores, ε_{bulk} is the dielectric function of the bulk material prior to porosification (i.e. silicon), and p is the porosity of the porous material (i.e., the volume fraction of air in the material). Once the effective dielectric function is known, the wavelength-dependent complex index of refraction can be found using the relations

$$\varepsilon = \varepsilon_1 + i\varepsilon_2 = (n + ik)^2 \ , \tag{28}$$

$$n = \sqrt{\frac{\sqrt{{\varepsilon_1}^2 + {\varepsilon_2}^2} + \varepsilon_1}{2}} \tag{29}$$

and

$$k = \sqrt{\frac{\sqrt{{\varepsilon_1}^2 + {\varepsilon_2}^2} - \varepsilon_1}{2}} \ , \tag{30}$$

where $\varepsilon_1$and ε_2 are the real and imaginary parts of the dielectric function, and n and k are the real and imaginary parts of the complex index of refraction. k is sometimes called the extinction coefficient; it is related to the absorption coefficient α by

$$\alpha = \frac{4\pi k}{\lambda} \ , \tag{31}$$

where λ is the wavelength in vacuum (not in the material). n and k are the material parameters needed by Sentaurus to calculate the optical transmission, reflection and absorption as a function of position within the solar cell structure.

3.2.2. Band Gap

The band gap of porous silicon can change significantly from that of bulk silicon, particularly in the case of nano-porous silicon where the crystallites are small relative to the carrier wave functions. In some cases the band gap of this type of porous silicon has been shown to be as large as 2 to 3 eV. In these cases quantum confinement also restricts the motion of carriers to the extent that the SRH recombination mechanism is greatly suppressed because carriers cannot move through the device and reach a recombination center where recombination would take place. As a result, radiative recombination can sometimes be the dominant process in nano-porous silicon.

Table 2: Reported properties of electron transport for *n*-type mesoporous silicon, and for the original *n*+ doped substrate the porous silicon was made from.

	Substrate	Porous Si
Electron Concentration (cm^{-3})	1.1x10^{18}	1.3x10^{13}
Electron Mobility (cm^{2}/V.s)	310	30
Resistivity (Ω.cm)	1.8x10^{-2}	1.6x10^{4}

In the meso-porous material being studied here though, which is porosified starting from a *p*+ doped silicon substrate, it is assumed that there is no significant quantum confinement; the wave functions of carriers are significantly smaller than the crystallites of silicon. The band gap is generally measured to be the same as that of bulk silicon [11, p. 204] and recombination through the SRH process is by far the dominant process due to the high concentration of crystal defects and surface states within the porosified material.

3.2.3. Carrier Transport

As was described briefly in section 2.1, carrier transport has been studied in meso-porous silicon, as well as in porous silicon/silicon structures, by several people. Simons [41] was able to report majority electron concentration and electron mobility for samples of meso-porous silicon made from *n*+ doped silicon substrates. This data is contained in Table 2. Timoshenko [14] reported similar data for meso-porous silicon made from *p*+ doped substrates, shown in Table 3. These values are adopted in Sentaurus for modelling *n*-type and *p*-type meso-porous silicon, respectively.

In both cases, the resistivity of the porous silicon is many orders of magnitude greater than the original substrate, despite the fact that porosity of the samples is on the order of 50%, and the

Table 3: Reported properties of hole transport for *p*-type mesoporous silicon, and for the original *p*+ doped substrate the porous silicon was made from.

	Substrate	**Porous Si**
Hole Concentration (cm^{-3})	$5x10^{18}$	$3x10^{17}$
Hole Mobility (cm^2/V.s)	83	$5x10^{-4}$
Resistivity (Ω.cm)	$1.5x10^{-2}$	$4.2x10^{4}$

typical meso-porous structures are strongly interconnected. In the case of *n*+ meso-porous silicon, the high resistivity is related to low carrier concentration in the porous material, while for *p*+ material the high resistivity is more closely related to low carrier mobility.

The cause of high resistivity has been a matter of some debate, but the consensus, as described by Timoshenko and others, seems to be that Si-H-B bonds and Si-O-H bonds form at the pore walls within the porous material. These bonds trap many of the electrons that would otherwise be free to conduct current within the material. Indeed, Balagurov showed a marked decrease in resistivity of porous silicon when the material is annealed above the activation energies of these bonds [42]. Timoshenko also reduced resistivity by an order of magnitude by filling the pores with a dielectric liquid, thereby modifying the local electric field within the porous network [14]. These experiments are useful to understand the cause of the high resistivity, and might also indicate a path toward improved device performance. It remains to be seen if the effect of annealing is durable, or would be lost over time as the bonds re-form on exposure to moisture and room temperatures.

3.2.4. Recombination

There are no data available to calibrate a model of Shockley-Read-Hall recombination within porous silicon material; however such is expected to be strongly present since the material is, by its nature, full of surface states and crystal defects. In order to be able to model performance of a device using this material, then, it is important that the porous silicon be located in an area of the device where SRH recombination will have little or no effect on performance. Lacking any accurate values for lifetime in porous material, the SRH lifetime parameters in the porous material are set to a conservatively low value of $1\text{x}10^{-11}$s, which is much shorter than lifetimes for any other material in a solar cell model. This short lifetime yields an extremely short diffusion length of ~ 10^{-4} μm, ensuring that any minority carriers generated in the porous silicon will quickly recombine without being collected. This short lifetime does not impede majority carrier transport in porous silicon of course, and so solar cell designs that rely only on majority carrier transport in porous material may still perform well, and should be modeled accurately using this approach.

Very recently, samples of GaAs grown on porous silicon have been fabricated for electrical characterization of the GaAs/porous Si/Si interface. Experimental measurements of these samples are currently being analyzed, and will be used to improve the modeling of porous silicon in Sentaurus, however they was not available in time to be included in this thesis.

3.3. Lifetime vs. Threading Dislocation Density

As described in section 2.2, growth of GaAs on lattice mismatched substrates results in threading dislocations in the grown material. These dislocations act as recombination centers where minority carriers recombine through a Shockley-Read-Hall (SRH) type of process with a lifetime inversely proportional to the threading dislocation density.

In the Sentaurus model, other recombination mechanisms (SRH, Auger, and radiative) are already included. The additional recombination due to threading dislocations can be included by modifying the SRH lifetime parameter in Sentaurus as

$$\frac{1}{\tau_{eff}} = \frac{1}{\tau_{SRH}} + \frac{1}{\tau_{TDD}}, \tag{32}$$

where τ_{eff} is the resulting effective lifetime for SRH-type processes, τ_{SRH} is the original SRH lifetime for good-quality material with low dislocation density, and τ_{TDD} is the lifetime for recombination through threading dislocations, which is calculated using (3). In this way, recombination due to threading dislocations is lumped in with the Shockley-Read-Hall process due to other defects such as dopants.

Figure 15 shows the calculated effective hole lifetime for *n*-type GaAs including the SRH processes using the lifetime calculated with (30), plus radiative and Auger processes. In this particular case, radiative and Auger processes are never very significant for any of the doping levels considered. For low threading dislocation density, the lifetime is relatively constant for low doping levels, but begins to decrease for a doping level above ~ $5 \times 10^{17}\text{cm}^{-3}$ where the mean distance between dopant sites becomes comparable with the diffusion length in un-doped material.

For higher dislocation densities, the hole lifetime drops significantly, especially at lower doping levels. For a given dislocation density there is a noticeable tendency for lifetime to increase as doping level increases, up to $1 \times 10^{18}\ \text{cm}^{-3}$. This is a result of the fact that mobility decreases with doping and hence carriers have a somewhat lower probability of reaching a recombination center. Above a doping level of 10^{18}, the lifetime may still be dominated by doping concentration and not threading dislocation density.

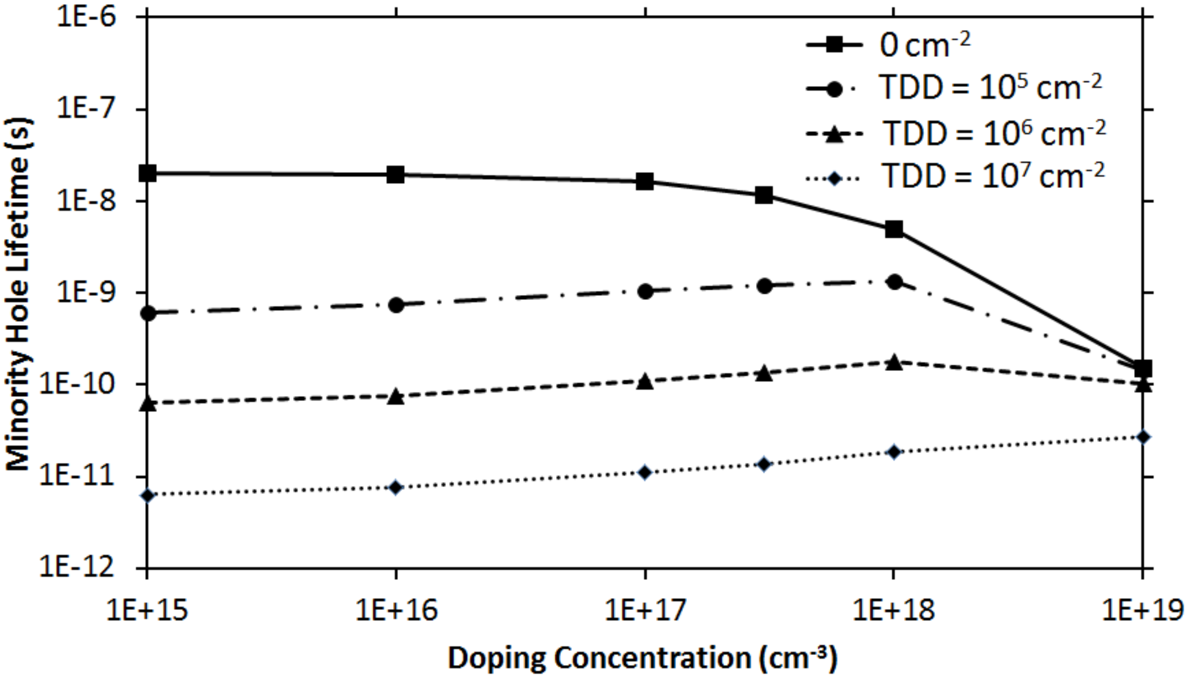

Figure 15: Calculated effective hole lifetime in *n*-GaAs for four different values of the threading dislocation density (TDD).

At this time, it is not known what threading dislocation density will be achievable in the grown GaAs, since the porosification and growth process is still under development. Based on measured XRD line-widths provided by Université de Sherbrooke, samples grown to date are estimated to have threading dislocation densities on the order of 10^8 cm^{-2} [6]. For the purposes of this study, a range of dislocation densities between 0 and 10^7 cm^{-2} have been studied, since we expect the porosification and growth process to improve.

3.4. Mobility vs. Threading Dislocation Density

It might be expected that threading dislocation density would have an impact not only on lifetime in a material, but also on carrier mobility. Similar to the case for minority carrier lifetimes, mobility in a material can be decomposed into the mobilities due to various scattering processes, as

$$\frac{1}{\mu}=\frac{1}{\mu_l}+\frac{1}{\mu_i}+\frac{1}{\mu_d}, \qquad (33)$$

where μ is the actual carrier mobility, and μ_l, μ_i and μ_d denote mobilities resulting from scattering by the lattice, impurities and dislocations respectively. In their analysis of thin-film GaAs solar cells on silicon substrates, Yamaguchi and Amano [43] estimated μ_d in GaAs based on earlier work by Dexter and Seitz [44], using the formula

$$\mu_d = \left(\frac{32kT\hbar}{3\pi E^2\lambda^2}\right)\left[\frac{1-\upsilon}{1-2\upsilon}\right]^2 (q/m^* TDD), \qquad (34)$$

where $E$is the deformation potential constant, λ is the unit crystallographic slip distance, υ is the Poisson ratio and m^* is the effective mass of the carrier. For TDD less than 10^8 cm^{-2} the reduction in mobility due to dislocations is small compared to changes in lifetime, and so any variation in mobility with dislocation density will not have a significant effect on diffusion length. For this reason, typical values for mobility in good-quality material are used for the materials epitaxially grown on porous silicon.

3.5. Choice of Solar Cell Structure

Before a device could be simulated, a specific starting point for the design must be chosen, taking into consideration constraints arising from the fabrication process as well as the efficiency of the final product. Some of the key design decisions are:

1. **Selection of an *n-p* or *p-n* structure.** The choice of device polarity can have a wide-ranging set of effects, since *n*-type and *p*-type materials frequently have different properties for similar doping levels. From a device performance point of view, different

lifetimes for electrons and holes may make one material preferable for use in the emitter or base of a subcell. At fabrication time, the different diffusivities of *p*-type and *n*-type dopants can make one polarity much easier to fabricate than another.

The *n-p* structure is most commonly used in multi-junction cells, and may be preferable for ease of fabrication. The *p-n* structure has, however, been shown to be more tolerant of the high density of threading dislocations expected in these devices, and has been demonstrated in some multi-junction solar cells grown by Fitzgerald's research group. Single-junction GaAs solar cells are typically designed with a *p-n* structure [22, p. 204]. In this project, the deciding factor was the existing fabrication technology at Université de Sherbrooke for making porous silicon [45]. The existing process can only be used to porosify *p*+ doped silicon. If a silicon subcell is to be located below the porous layer, then, the subcell must have a *p-n* structure. It follows that the entire multi-junction cell will have a *p-n* structure.

2. **Number of junctions, and materials to use for those junctions.** Under ideal conditions, the maximum possible efficiency increases with the number of junctions in the device, however in order to achieve this, the photocurrent must be balanced in each of the subcells. Traditional GaInP/GaAs/Ge triple-junction solar cells collect roughly twice as much current in the 0.67 eV Ge subcell as in the other two subcells, and this extra collected current is largely wasted. A more optimal design would have a bottom subcell with a bandgap of around 1.0 eV [46]; this would collect sufficient current to match the top two subcells and would provide more voltage at the maximum power point than would a Ge subcell. Silicon has a bandgap of 1.12 eV, and so a 3-junction,

GaInP/GaAs/Si structure was selected for the focus of this work, with the aim of providing a better current match than the 3-junction cell on germanium while also using a lower-cost substrate.

Since the bandgap of silicon is greater than the optimum 1.0 eV, it is expected that the bottom subcell will limit the short-circuit current of the device, unless the top subcells are thinned to transmit some shorter-wavelength light through to the bottom subcell.

3. **Thickness of the porous silicon layer.** Since the porous silicon is known to be highly resistive, it is desirable to use as thin a layer as possible to minimize the series resistance of the final device. Thinning the porous layer also reduces the thermal resistance of the porous layer. Some minimum thickness will however be required to provide the desired compliance at the interface between silicon and GaAs lattices. Additionally, the large difference in index of refraction between porous silicon and the other cell materials can result in reflection of light that would otherwise reach the bottom subcell. For reference, the index of refraction n of porous silicon can approach 1.0 for high porosities (an exact value can be obtained from equations (25-28)). GaAs and silicon both have $n \sim 3.55$ in the range of wavelengths that must be transmitted to the bottom subcell.

   If we consider the GaAs/porous silicon/silicon layer structure in Figure 16, where ${A_0}^+$, ${A_2}^-$, ${B_0}^+$ and ${B_2}^-$ represent the amplitudes of incident and reflected plane waves in the GaAs and silicon layers, then the transfer matrix method (TMM) can be used to derive an equation relating the field strength transmitted through the porous silicon to the field strength incident on it [27, p. 522] as

$$\begin{bmatrix} B_0{}^+ \\ A_0{}^+ \end{bmatrix} = \frac{1}{2n_0}\begin{bmatrix} n_0+n_1 & n_0-n_1 \\ n_0-n_1 & n_0+n_1 \end{bmatrix}\begin{bmatrix} \exp\left(\frac{2\pi i n_1 d}{\lambda}\right) & 0 \\ 0 & \exp\left(\frac{-2\pi i n_1 d}{\lambda}\right) \end{bmatrix}\frac{1}{2n_1}\begin{bmatrix} n_1+n_2 & n_1-n_2 \\ n_1-n_2 & n_1+n_2 \end{bmatrix}\begin{bmatrix} A_2{}^- \\ B_2{}^- \end{bmatrix}, \qquad (35)$$

where, n_0, n_1 and n_2 are the complex indices of refraction of GaAs, porous silicon and silicon, respectively, d is the thickness of the porous layer, and λ is a specified wavelength (in vacuum). By setting the amplitude of the wave incident on the porous layer from GaAs, $A_0{}^+$, to 1 and the amplitude incident on the porous layer from silicon, $A_2{}^-$, equal to zero, we can solve for the reflected and transmitted wave amplitudes $B_0{}^+$ and $B_2{}^-$ relative to $A_0{}^+$. The transmitted and reflected optical intensities, again relative to the incident intensity, are then given by

$$I_{trans} = \frac{real(n_2)}{real(n_0)}\|B_2{}^-\|^2 \qquad (36)$$

and

$$I_{refl} = \left\|B_0{}^+\right\|^2 . \qquad (37)$$

Figure 17 shows the calculated relative transmission and reflection for three different thicknesses of porous silicon: 0.35, 0.70 and 0.90 µm. The silicon subcell is only expected to absorb light within the wavelengths of 0.9 to 1.1 µm, since light of shorter

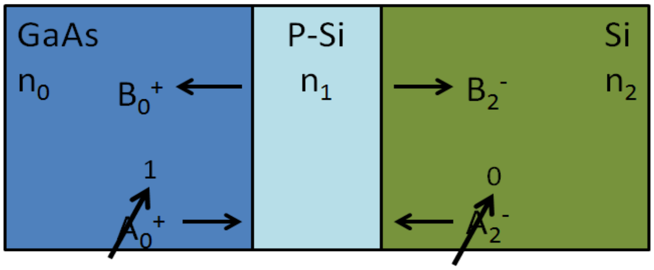

Figure 16: Simple model for transfer matrix method analysis of optical transmission through the porous silicon layer.

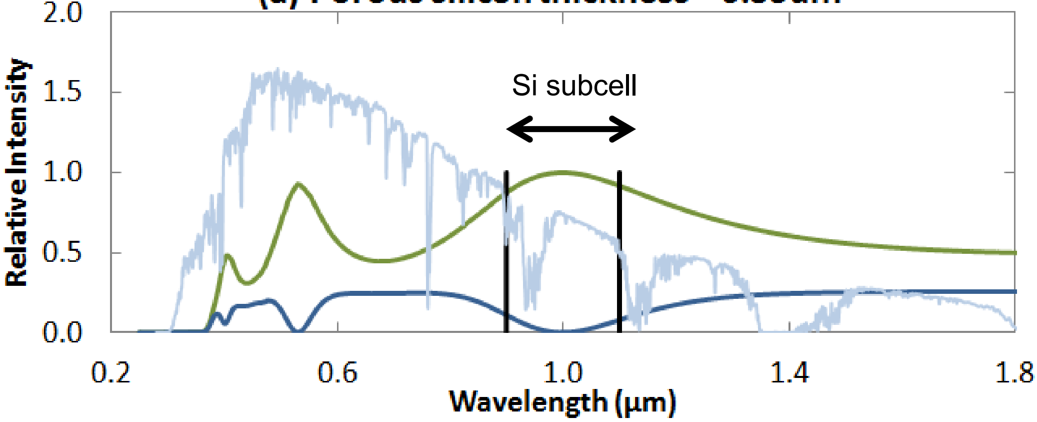
(a) Porous silicon thickness = 0.35um

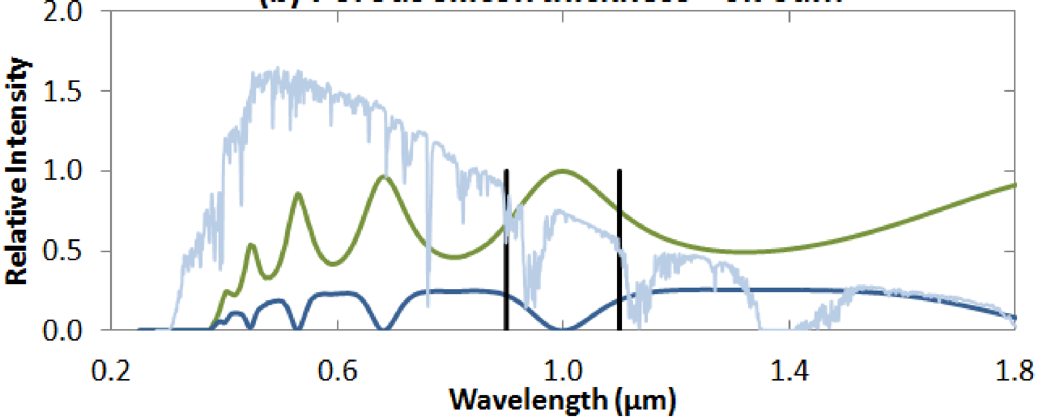
(b) Porous silicon thickness = 0.70um

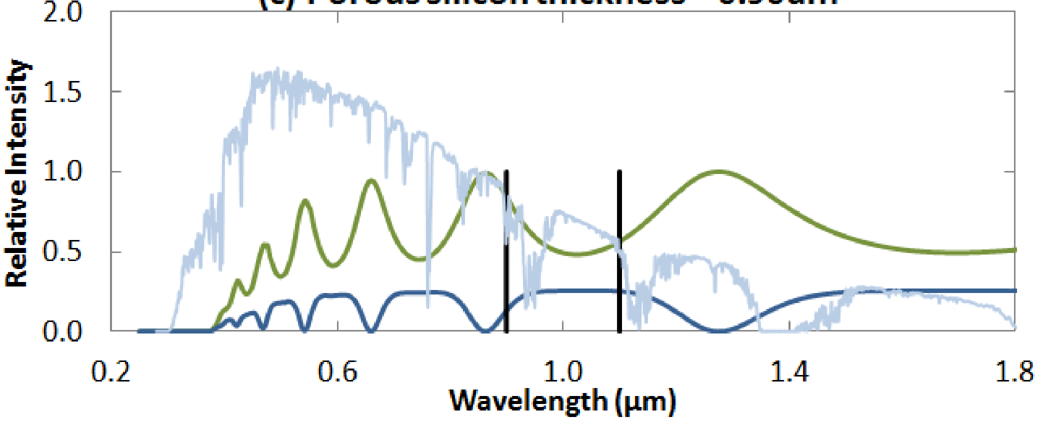
(c) Porous silicon thickness = 0.90um

Figure 17: Relative optical transmission (green) and reflection (blue) of the porous silicon layer. The design must be optimized to maximize transmission in the range of wavelengths that will be absorbed by the silicon subcell, between 0.9 and 1.1 um (black lines). For reference, the AM1.5D spectral irradiance is shown with arbitrary units.

wavelength will have been (mostly) absorbed by the GaAs subcell, and longer wavelengths have too little energy for the 1.12 eV band gap of silicon. Since we expect that the silicon subcell will limit the short-circuit current of the multi-junction device, it is very important to maximize optical transmission through the porous layer in order to increase current generation in the silicon subcell as much as possible.

Thicknesses of 0.35 and 0.7 μm provide transmission peaks centered in the wavelength range of the silicon subcell, while a thickness of 0.9 μm results in a minimum in the relevant wavelength range. As a starting point for this study, a 0.35 μm thickness was chosen based on the simple TMM analysis shown above. This initial thickness was later refined during the optimization process that will be described in section 3.6, below.

3.6. Design Optimization

In order to present the most interesting and useful results for the proposed solar cell design, it is important to optimize the design for maximum efficiency. A solar cell design of this type has a very large number of adjustable parameters – perhaps 80 or more if doping levels, thicknesses and material compositions of all layers are considered. Additionally, the optimization problem can be highly nonlinear with local extrema and varying sensitivity to a given parameter depending on the position within the solution space. For this type of global optimization problem, there is no algorithm that can be guaranteed to find the globally optimum solution. It should also be noted that the various design parameters are highly interlinked; for example, a change in the ARC design might increase transmission to the silicon subcell at the expense of the GaInP subcell. This could be compensated by other factors, such as thickening the GaInP subcell at the expense of the other two subcells. In general, it is not possible to start with an 'optimal' ARC design and then design the other components around it; each of the components is dependent on the performance of the others.

The Sentaurus Workbench program, which serves as a user interface for the various tools that comprise Sentaurus, includes an optimization tool that allows a series of simulations to be run with varying parameters in order to optimize some specified objective function. The tool includes both relatively simple optimization algorithms and more sophisticated methods such as a genetic algorithm, which should be effective for problems involving large numbers of parameters and highly nonlinear behaviour.

It would be very desirable to establish a more standardized method of performing an optimization. For example, if two alternative designs are being compared, it would be useful to be able to subject both designs to a similar optimization routine in order to provide a fair comparison. To date, researchers at SUNLAB have typically found an ad-hoc approach, manually optimizing one or two parameters at a time, to give the most effective results in optimizing a given design. No standard method of performing an optimization has yet been established.

In practice, optimization is usually done with a simplified, one-dimensional (1D) version of the cell model in order to allow more design iterations to be run in a given amount of time. The ad-hoc approach involves selecting a single parameter at a time and running simulations with five or more trial values. If a peak in performance is found, that value will be adopted for the next set of optimization, otherwise a new set of parameter values will be tried until a peak is located. Using this technique, many parameters can be optimized, however there is often a strong interdependence between various parameters, and so each parameter must be optimized several times to finally reach a locally optimum set of parameters. This approach is similar to a gradient-search type of algorithm, and as such it generally will only find local maxima of cell efficiency. For that reason it is very important to initiate the optimization with a good set of initial parameters, based on understanding of the device operation or reported values from literature.

The optimization tool in Sentaurus Workbench includes a variety of optimization algorithms, such as gradient-descent methods, and a genetic algorithm that should be effective for problems involving large numbers of parameters and highly nonlinear behaviour. Ideally these algorithms could be used to perform a 'hands-off' optimization over a very large set of parameters. Unfortunately, it seems to be impractical to assign more than ~10 parameters to be optimized at any one time, or to give the optimization tool wide latitude in the range of parameter values, as this tends to lead to solutions with very poor performance and no clear gradient toward higher performance. It also tends to produce parameter combinations that fail to converge at all, or that take an excessively long time to converge to a solution.

Despite the limitations described above, the genetic algorithm was able to find a parameter combination with greater efficiency than a purely ad-hoc approach. The genetic optimization tool proceeds by generating a 'population' of experiments, randomly choosing parameter values from within an allowed range prescribed by the user. The efficiencies are evaluated, and the cell designs with highest efficiencies are selected to form the population for the next generation of designs. Population diversity expresses new designs by a combination of 'mutation' – randomly altering a parameter in one of the existing high-performance designs, and 'cross-breeding' –

combining some of the parameters from one successful design with other parameters from another, in hopes of finding a design that provides the advantages of both. In order to test the genetic optimization tool, a 1D simulation was set up with the parameters specified in Table 4.

Table 4: Parameters specified for design optimization.

Parameter	**Min Value**	**Max Value**
Top subcell base thickness	0.1	0.3
Middle subcell base thickness	0.25	0.65
Bottom subcell base thickness	250	380
Porous layer thickness	0.3	0.7
Buffer layer thickness	0.3	0.7
ARC MgF layer thickness	0.09	0.13
ARC TiO_x layer thickness	0.05	0.09

Options were set to re-use the 10 highest efficiency designs to generate the next population. The highest-efficiency 1D design that was known prior to genetic optimization had an efficiency of 31.7%, and this was provided as an input for generating new iterations. The optimization tool ran for approximately 28 hours, producing 7 generations and approximately 700 design iterations before it stopped due to a technical issue (Figure 18).

The first generation of designs had quite low performance compared with the previously known, manually optimized design. Starting from the second generation, though, performance was much better and eventually exceeded the performance of any previously known design. In the final generation before the optimizer was stopped, a single design with an efficiency of 32.2% was found; this particular design is well above the next closest competitors and shows that although the trend is toward a leveling-out of the efficiency of new iterations, there are still some new parameter spaces to explore. Further generations would have included mutations and crossbreedings of this 32.2% efficient design, and presumably would have produced a range of designs with similar, or perhaps even better, efficiency. It would be possible to optimize the design further by allowing variation in other parameters such as emitter thicknesses, doping levels and parameters of the front and back surface fields.

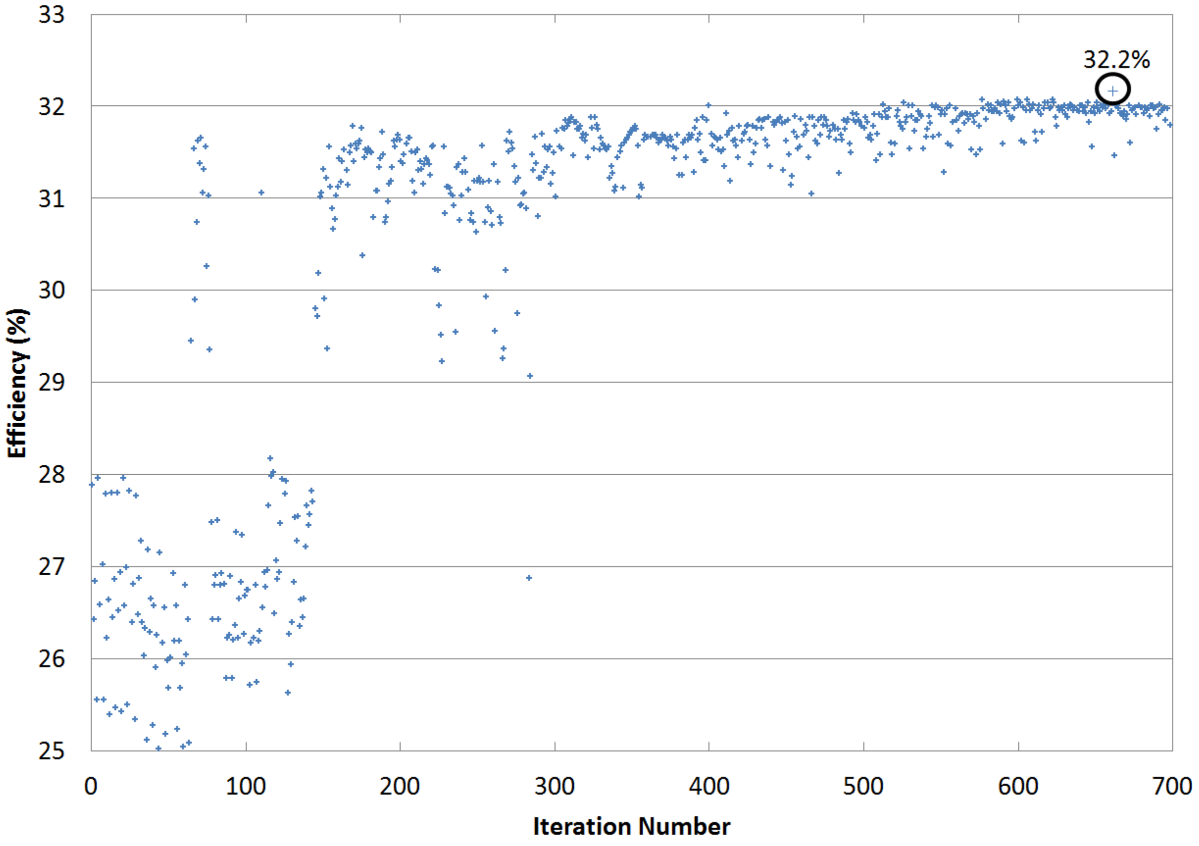

Figure 18: Efficiency of cell designs generated using the genetic optimization tool in Sentaurus. After approximately 28 hours and 660 iterations, the optimizer found a 32.2% efficient 1D design, an increase of 0.52% (absolute) over the best previously known design.

4. Results and Analysis

This chapter presents the final multi-junction solar cell design that resulted from the iterative optimization procedure described in section 0, and describes the simulated performance results. The performance is compared against competing technologies, and some of the technological factors that limit performance and influence the possible applications of this type of solar cell are discussed.

4.1. Result of Optimization Process

As described in section 0, two optimization methods were tried: (1) a manually operated method where one parameter at a time was selected and a range of values was tried in order to find a maximum efficiency point, and (2) an automated genetic optimization algorithm using the optimization tool built into Sentaurus Workbench. For both methods, many parameters were varied including doping levels, material thicknesses and also the material compositions (mole fractions) of certain layers.

The result of the optimization process is presented in Table 5; the design contains a total of 21 layers including an anti-reflective coating, a cap layer to help produce a good ohmic contact at the anode, GaInP, GaAs and Si subcells each with front and back surface fields, and AlGaAs/GaAs tunnel junctions located in between the subcells. It would be valuable to study the sensitivity of the model to each of the design parameters. In particular, the thickness of the porous silicon layer is expected to be a sensitive parameter. Also, variations in the subcell thicknesses can upset the current balancing and have a significant effect on performance.

Table 5: The multi-junction solar cell design resulting from the optimization process.

	Material	Thickness	Doping
ARC	MgF_2	0.11 µm	
	TiO_x	0.07 µm	
Cap	GaAs (etched away except under contacts)	0.20 µm	*p* $1x10^{19}$
Top Subcell	$Al_{0.5}In_{0.5}P$	0.03 µm	*p* $8x10^{18}$
	$Ga_{0.5}In_{0.5}P$	0.05 µm	*p* $2x10^{18}$
	$Ga_{0.5}In_{0.5}P$	0.20 µm	*n* $8x10^{17}$
	$Al_{0.5}In_{0.5}P$	0.03 µm	*n* $1x10^{19}$
Top TJ	$Al_{0.8}Ga_{0.2}As$	0.03 µm	*n* $2.5x10^{19}$
	GaAs	0.03 µm	*p* $2.5x10^{19}$
Middle Subcell	$Al_{0.8}Ga_{0.2}As$	0.04 µm	*p* $1x10^{19}$
	GaAs	0.22 µm	*p* $3x10^{18}$
	GaAs	0.39 µm	*n* $1x10^{18}$
	$Al_{0.2}Ga_{0.8}As$	0.04 µm	*p* $1x10^{19}$
Bottom TJ	$Al_{0.8}Ga_{0.2}As$	0.03 µm	*n* $2.5x10^{19}$
	GaAs	0.03 µm	*p* $2.5x10^{19}$
	$Al_{0.65}Ga_{0.35}As$	0.50 µm	*p* $1x10^{19}$
	Porous Si	0.50 µm	*p* $3x10^{17}$
Bottom Subcell	Si	0.05 µm	*p* $5x10^{19}$
	Si	0.50 µm	*p* $1x10^{18}$
	Si	315 µm	*n* $2x10^{16}$
	Si	1.0 µm	*n* $3x10^{19}$

4.2. Simulated Cell Performance

Each of the standard methods that are used for experimentally measuring solar cell performance, such as *I-V* curves and external quantum efficiency, can also be implemented in the simulation environment. These techniques provide significant insight into how the cell is performing and what physical processes are limiting the device's performance. In addition, the simulation makes it possible to probe the device performance in ways that are not directly measurable, such as by examining energy band diagrams and by calculating the bulk recombination rate within certain regions of the semiconductor material. These techniques have been used to study the performance of the optimized cell design, to understand what may be limiting its performance, and to find avenues for further improvement.

4.2.1. Subcell *I-V* curves and Current Matching

By inserting virtual 'contacts' in the simulation at planes between the subcells, it is possible to apply bias to subcells individually and so generate *I-V* curves for each one, as it operates within the complete device. This type of measurement typically cannot be done by direct experiment – though at least one research group has inferred subcell *I-V* curves from electroluminescence measurements [47]. Since the subcells operate in series with one another, they must be designed to operate efficiently while all operating with the same current. Ideally, the design should be optimized so that all subcells can be simultaneously operating at their maximum-power current (I_{mp}) [48] This implies, of course, that the I_{mp} of each of the subcells should be equal.

In practice, GaInP/GaAs/Ge multi-junction cells typically have their top and middle subcells (nearly) current-matched, but the bottom Ge subcell produces almost twice as much current as the others. This is not the case for a GaInP/GaAs/Si solar cell; the cell can be designed such that all three subcells are current matched at their respective maximum power points (Figure 19).The solid lines in the figure represent *I-V* curves of 1D simulations of the GaInP, GaAs, and Si subcells with the threading dislocation density parameter set to 0 cm^{-2}. The silicon subcell shows a noticeable series resistance, apparent from the reduced slope of its *I-V* curve at open-circuit. This is because the porous silicon interface region has been included in the silicon subcell; as noted earlier, porous silicon is modeled with a resistivity of $\rho = 4.2\text{x}10^4$ Ω.cm, leading to a series resistance of 2.1 Ω.cm^2 for a 0.5μm thick layer. Under 1-sun conditions this leads to a 25 mV drop in voltage, or 0.7% of the open-circuit voltage of the multi-junction solar cell. This will be

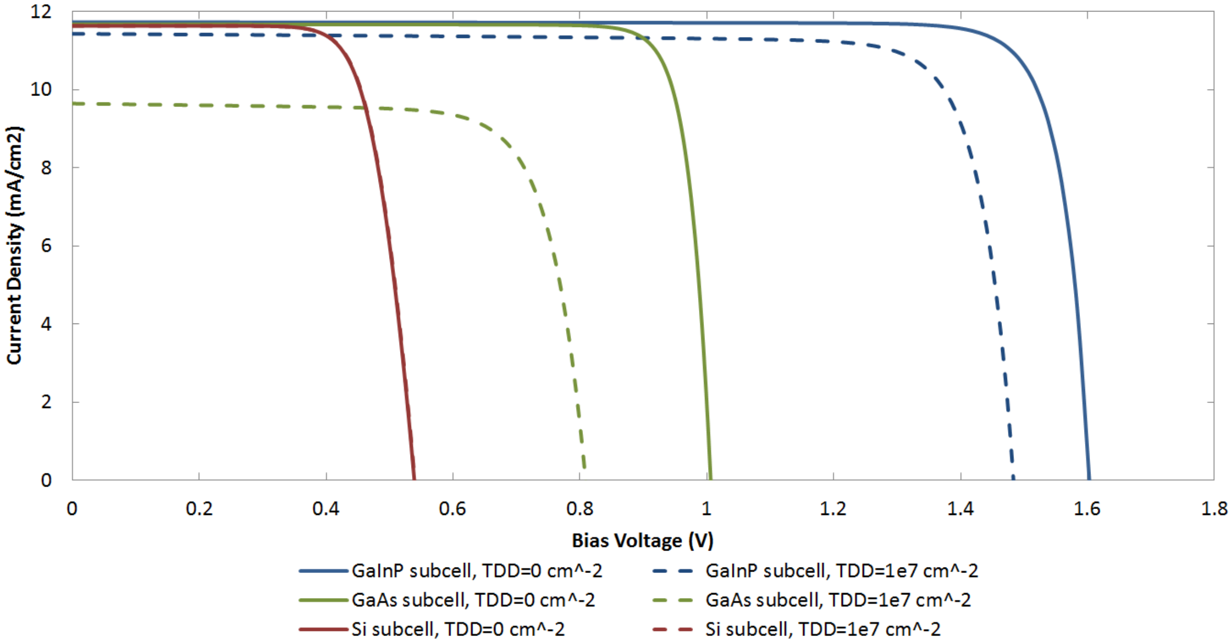

Figure 19: *I-V* curves of individual subcells of the multi-junction solar cell. Solid curves correspond to a simulation with threading dislocation density (TDD) set to 0 cm^{-2}. Dashed curves are for TDD=10^7 cm^{-2}.

discussed further in section 4.2.3 on the effect of concentration. The dashed lines in Figure 19 show how the subcell *I-V* curves change with the addition of threading dislocations, and the resulting increase in the SRH recombination rate. The silicon subcell is unaffected, since threading dislocations are only considered in the top two subcells. The GaInP and GaAs subcells, however, show significant reduction in open-circuit voltage and short-circuit current.

The change in open-circuit current with TDD is directly related to changes in internal quantum efficiency (Figure 20). It is clear that at TDD = 10^7 cm^{-3}, the IQE of the GaAs subcell is greatly reduced. Since the subcells were current-matched at TDD = 0, the GaAs sub-cell must be severely limiting for the high TDD case. It appears, because the diffusion lengths in the GaAs base and emitter are already somewhat short compared to the GaAs subcell thickness, that the GaAs subcell is particularly sensitive to further reduction in diffusion length due to dislocations.

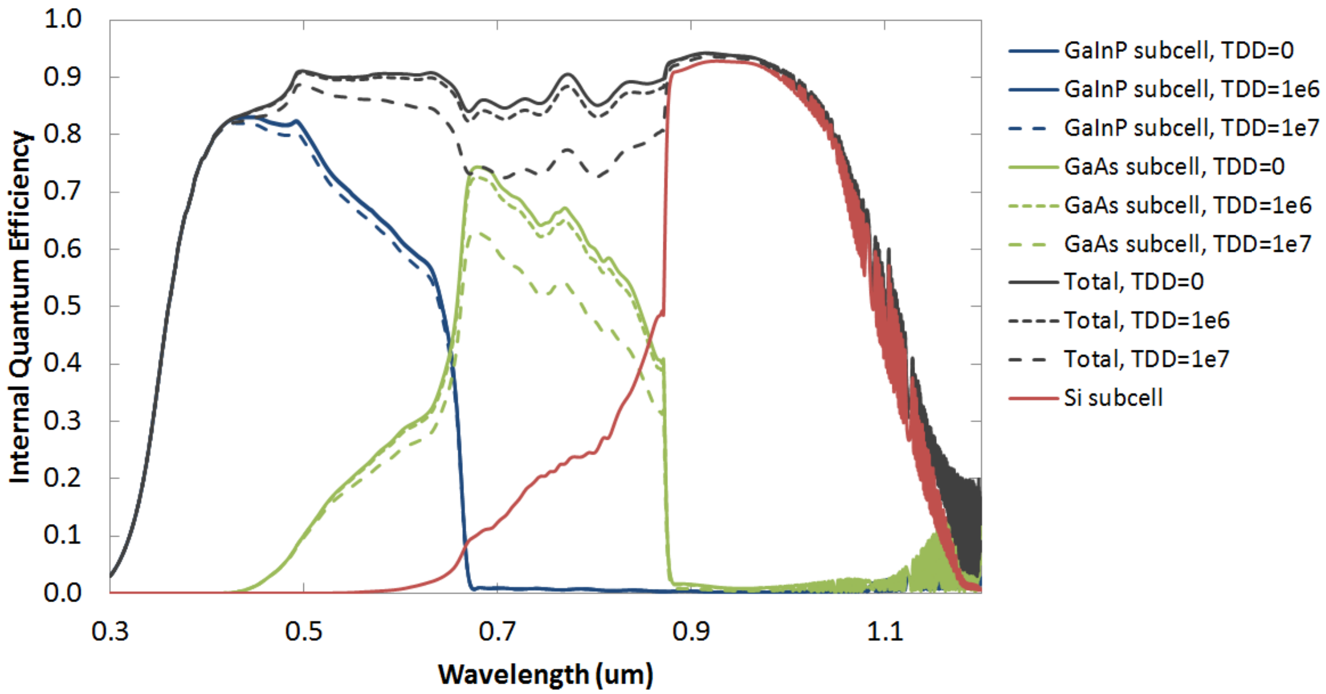

Figure 20: IQE of GaInP/GaAs/Si cell design. Increasing TDD has a much stronger effect on QE of the GaAs subcell compared with the other subcells.

We should note here that the cell design presented here was optimized for the TDD = 0 case. Judging by the IQE plot shown here, it is likely that the design could be re-optimized for a specific, higher value of TDD to obtain improved current matching (and hence improved efficiency) for that value of TDD. To date, the best values of TDD produced experimentally are greater than 10^7 cm^{-2}, but efforts to improve crystal quality are continuing.

4.2.2. Light *I-V* Curve of Complete Cell

The definitive measure of the performance of a solar cell is a plot of its *I-V* curve. With the solar cell under illumination, the point under the *I-V* curve with the maximum product of current and voltage is called the maximum power point; this is the optimal operating point where the solar cell produces maximum electrical power under the test conditions. The light *I-V* curve can also provide information about series or shunt resistances that may be present in the device. Since the porous silicon material is expected to have significant resistance, series resistance is of particular interest in this project and will determine the maximum level of concentration under which the cell can be used. A low fill factor can be a result of several things, including a high series resistance, a low shunt resistance, or poor material quality in the solar cell.

Table 6: Simulated *I-V* parameters for the optimized solar cell design, for varying values of threading dislocation density (TDD).

	TDD (cm^{-2})			
	0	**10^5**	**10^6**	**10^7**
J_{SC} (mA/cm^2)	10.96	10.96	10.89	9.83
V_{OC} (V)	3.27	3.23	3.13	2.93
***FF* (%)**	85.6	84.3	82.8	82.3
Efficiency (%)	30.7	29.9	28.2	23.7

The simulated *I-V* parameters are given in Table 6, and show an efficiency of 30.7% with no threading dislocations (TDD=0), decreasing to 28.2% with TDD=10^6 cm^{-2} and 23.7% with TDD=10^7 cm^{-2}. For lower values of TDD, loss of efficiency occurs mostly through reduction of the open-circuit voltage; this is expected, as threading dislocations cause increased SRH recombination which increases the cell's dark current and results in reduced voltage. At the highest threading dislocation densities, recombination also impacts the collection of carriers under short-circuit conditions.

The same effects can also be seen in the *I-V* curves, shown in Figure 21. At the highest TDD value, there is a small slope in the curve at low bias, similar to the typical appearance of an *I-V* curve of a cell with low shunt resistance. A curve of this type can also occur in cells with extremely short minority carrier diffusion length where carrier collection is aided by drift in the electric field at the junction [49]. This may be the case in the GaAs subcell which is current

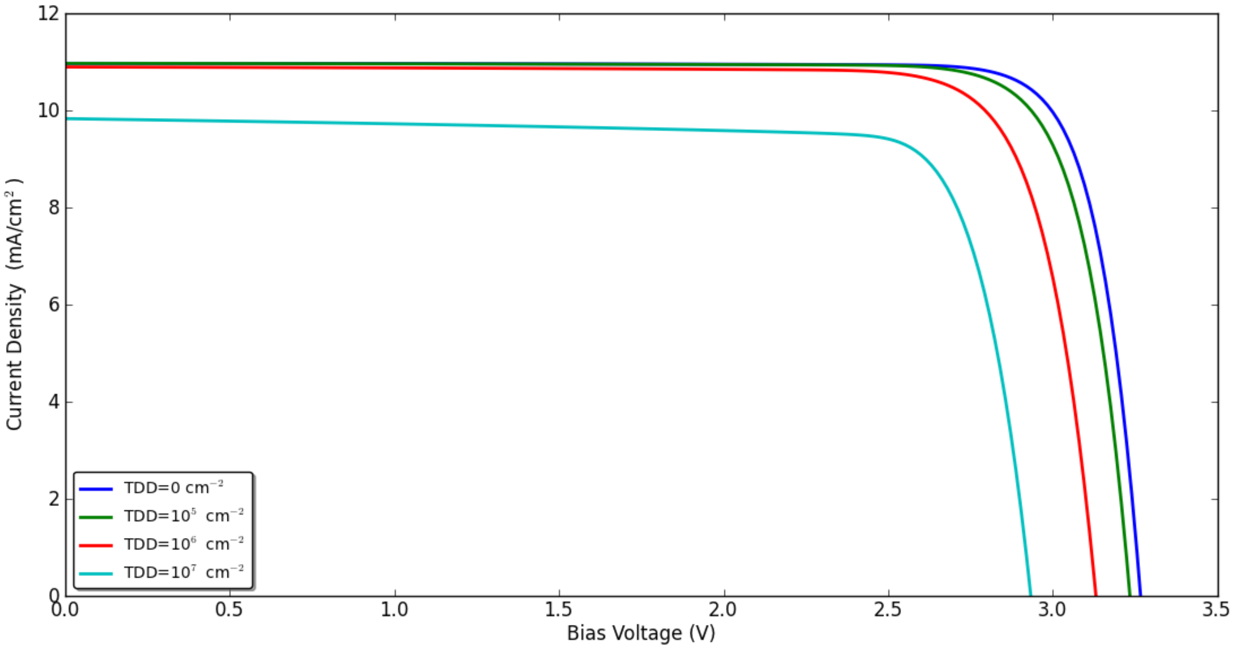

Figure 21: *I-V* curves of the complete GaInP/GaAs/Si solar cell for various values of threading dislocation density (TDD). AM 1.5G spectrum, 1-sun, cell temperature 25°C.

limiting at TDD = 10^7 cm^{-2}.

4.2.3. Effect of Concentration

From the beginning of this project it was expected, based on simple calculations using the resistivity of porous silicon material, that series resistance would preclude operation of these devices under high concentration. Indeed, *I-V* curves showing simulated cell performance under concentration (Figure 22) show a slope where the curve intersects the voltage axis that is characteristic of series resistance. This effect in itself would be sufficient to preclude operation at high concentration, as the voltage drop associated with the series resistance would be

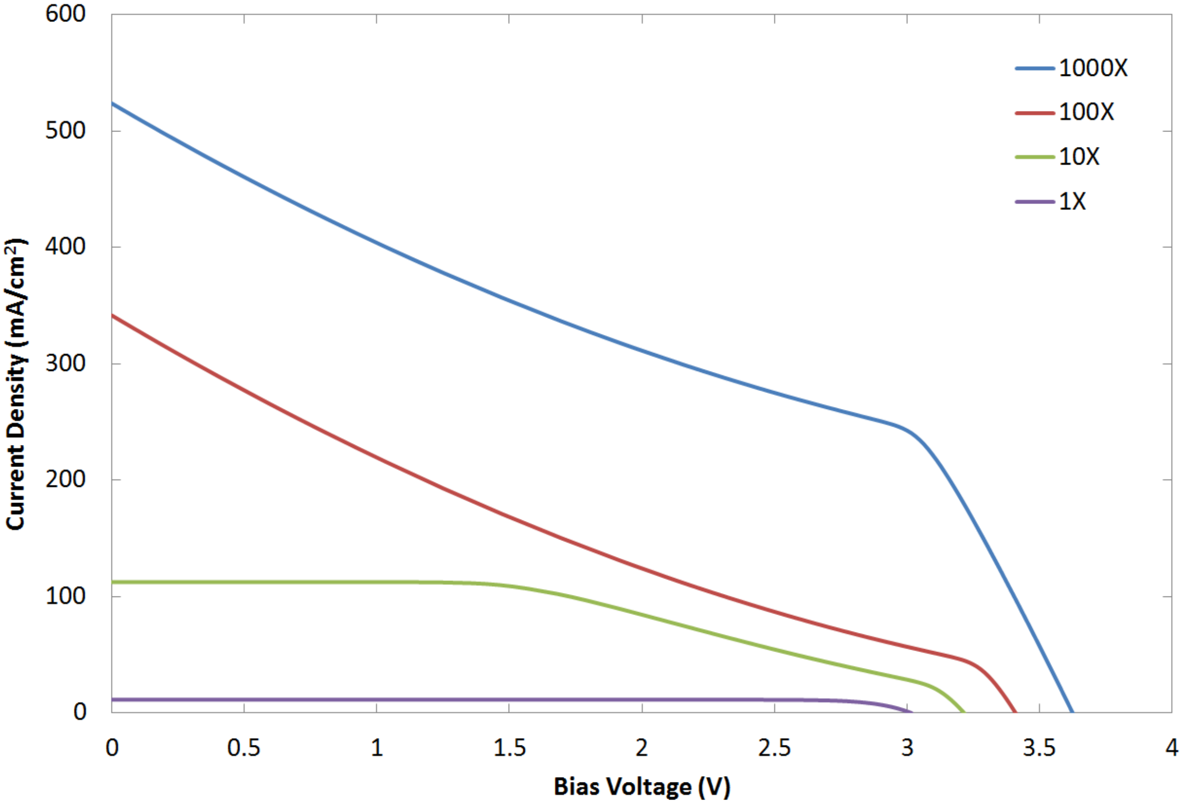

Figure 22: *I-V* curves with TDD=0 cm^{-2}, at various illumination intensities. The shape of the *I-V* curve is normal at 1-sun, but quickly becomes distorted at higher concentrations.

comparable with the open-circuit voltage of the device. A reduction in resistivity by a factor of approximately 200 would be required to make these devices viable under concentration.

In the plot, though, there is an even larger effect evident as a 'bevel' in the *I-V* curve. At 10X concentration, the bevel is mainly in the area near maximum power point, but at higher concentrations it is present over most of the *I-V* curve and reduces the short-circuit current of the device to far less than a linear scaling of the 1-sun short-circuit current. (The 1-sun short-circuit current is 11.1 mA/cm^2, so a linear scaling should result in 11100 mA/cm^2 at 1000X concentration; instead we only see 520 mA/cm^2).

Some further study is required to understand the precise nature of this beveling of the *I-V* curves under concentration, as it does not fit within the traditional two-diode model of solar cell operation. One possibility is that there is a potential barrier formed at the porous silicon/III-V interface; this type of problem could be identified by studying the potential drop through the device as a function of concentration.

Finally, it should be noted that the series resistance of the porous silicon material shown here is based on the best available data in the literature, but it is known that, like other material properties, the resistivity of porous material varies strongly with preparation conditions. Two studies, one involving filling the pores of the material with different dielectric liquids [14] and one involving annealing to break Si-H-B and Si-O-H bonds that form at the pore surfaces [42], have shown reductions in resistivity of an order of magnitude or more. These studies offer some hope that cells using porous material could be applied under high concentration, however it is not known if the annealing or pore-filling techniques would be fully compatible with other fabrication processes required to make solar cells.

4.2.4. External Quantum Efficiency

Plots of the simulated EQE (Figure 23) and IQE (Figure 20) show significant overlap in the wavelength response of the individual subcells. This is unusual compared with most multi-junction cell designs, but is a result of significantly thinning the top two sub-cells to transmit the required amount of light to the bottom sub-cell in order to achieve current-matching. There is also a significant oscillation in the EQE of the silicon subcell, particularly near the band edge at 1.12 µm. Recent studies by Olivier Thériault, done after this modeling work was performed, suggest that this could be a result of an unrealistic modelling of reflections from the back surface of the simulated silicon wafer. His work suggests that it would be more realistic to model reflections at the back surface with a diffuse Lambertian reflection (reflecting equal power at all angles) rather than the direct reflection that is produced by default in the TMM calculation. The

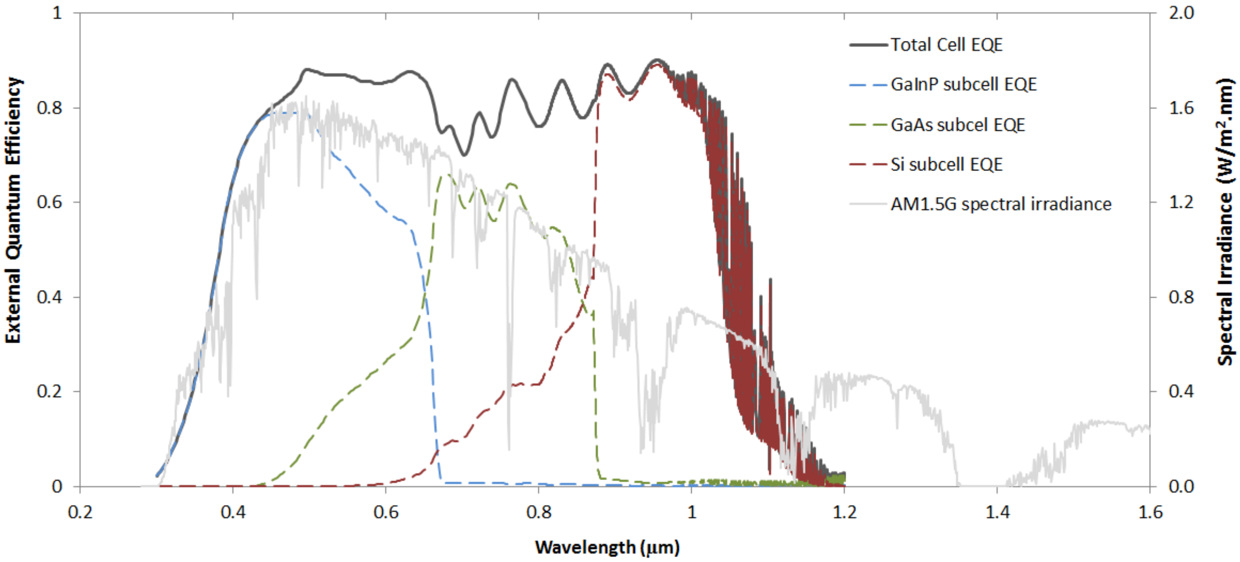

Figure 23: Simulated EQE of the multi-junction solar cell design on silicon substrate for TDD = 0. Note significant overlap in the response of different subcells; this is due to the thinning of the top two subcells to achieve current matching.

oscillations would also be ‘averaged out’ if a distribution of incident angles were considered rather than strictly normal incidence.

4.3. Comparison with Standard Multi-junction Solar Cells and Silicon Solar Cells

Compared with other existing solar cell technologies, the cell design presented here has potential for higher efficiency than any cell made to date on a silicon substrate [1]. Silicon cells in large scale production today have an efficiency of approximately 15%, while some premium priced silicon cells are produced with efficiency of 20-22% [50]. In the laboratory, a silicon cell with efficiency of 25.0% has been demonstrated [1]. Multi-junction devices on germanium substrates are commercially available with efficiency of 29.5% at 1-sun [51], and an efficiency of 32.0% at 1-sun has been demonstrated in the lab [52]. These results are summarized in Table 7.

Table 7: Efficiency of various solar cell technologies

	SJ Silicon (typical)	**SJ Silicon (premium)**	**MJ on Ge substrate**	**MJ on Si substrate (this work)**
Efficiency	~15%	25%	32.0%	28.2% (TDD=10^6cm^{-2})

It is expected that the MJ on Si type of cell will be as expensive, or perhaps not much more expensive, than the existing premium silicon solar cell technologies that yield efficiencies of 25%. So, initial efforts to develop this technology should target efficiency greater than 25%, which will require material with threading dislocation density (TDD) in the range of 10^6 - 10^7 cm^{-2}. While experimental results are not in this range yet, the process of growth on porous silicon is being refined and it is not unrealistic to expect that this level could be reached. The comparison with existing technologies would be much more compelling if the issues that are currently limiting operation under concentration can be resolved.

5. Conclusions and Recommendations

Initially, the multi-junction GaInP/GaAs/Si solar cell technology studied here will be limited to operation at 1-sun. Under those conditions, the simulations show an efficiency of 30.7% under the AM1.5G spectrum for material with low TDD, decreasing to 28.2% for TDD = 10^6 cm^{-2} and 23.7% for TDD = $10^7 cm^{-2}$. Further work is required to demonstrate the necessary material quality, however there have been some encouraging results using other, similar methods for growth of GaAs on silicon [10, 53, 54]. With some advances in material growth and fabrication, combined with further improvements and optimization of the design, the solar cell technology presented here has potential to be a competitive, lower-cost option compared with existing multi-junction cells. The initial study presented here is complete, but there are many avenues for continued research in this area, as well as improvement of the simulation process.

It is always good practice to validate models against physical measurements, and to this end it would be extremely useful to have access to more devices like the GaAs test structures discussed here where the entire layer structure of the device is known. Also, in order to be able to make meaningful comparisons between models and experiments, the devices must have minimal ‘unknowns’. Passivating the side surfaces of test structures is highly recommended, as any recombination at the side surfaces is likely to obscure the behaviour that is of greatest interest.

Recently, the group at CRN^2 has produced material samples of GaAs epi-layers grown on porous silicon, with electrical contacts applied. These samples can be used to verify and/or improve the material models that are implemented in this work, and will be essential to further work in simulating these devices. The optical properties of the material, conductivity, and the as-yet unknown issue of arsenic diffusion into the porous silicon should be investigated in detail. Also, the methods of improving conductivity of porous silicon through filling with dielectric liquid [14] and annealing to reactivate dopant atoms [42] warrant further investigation. These approaches could lead to operation under concentration, which would greatly increase the range of possible applications for these devices.

Compared with conventional lattice-matched multi-junction solar cells, this design has two aspects which might raise questions with respect to reliability: the porous layer and the high dislocation density of the III-V material. Solar cells with metamorphic (non-lattice matched) structures have been successfully qualified for space applications, including stringent requirements on reliablility, so the high dislocation density is not expected to be problematic here. The reliability of the porous layer, however, is a question which bears further investigation and is beyond the scope of this work.

In order to achieve better performance from a multi-junction III-V solar cell on silicon, it would be worthwhile to study materials other than GaInP and GaAs. These materials are frequently used due to the ease of growing them on GaAs and Ge substrates, but having broken the requirement for lattice matching to the substrate, a wide range of other materials could be explored. Other technologies for growth of III-Vs could also be explored; the method described in [54] could be very suitable and to date has demonstrated lower TDD than growth using porous silicon.

Appendix A. Material Properties of Selected Semiconductor Device Materials

A.1. Material Models

Presented here are nominal material parameters at 300 K for the most important active materials used in solar cells, as used in this project. This section is written for the benefit of future users of Sentaurus, and to that end it includes some references to Sentaurus commands and parameters that may not be familiar to all readers. Also, it focuses on material parameters where there are several possible choices available or where there the default values in Sentaurus are not appropriate. Many material models in Sentaurus are named after the author of the relevant publication. The model name will be placed in quotes, i.e. 'Altermatt', to indicate a reference to the model as it has been implemented in Sentaurus, and not the author or the original publication.

Table 8: Basic Parameters at 300 K

	$Ga_{0.51}In_{0.49}P$	**$Al_xGa_{1-x}As$**	**GaAs**	**Silicon**	**Germanium**
Bandgap E_g (eV)	1.84 Direct	1.72 (x=0.2) direct 2.10 (x=0.8) indirect	1.424 direct	1.124 indirect	0.661 Indirect
Electron affinity χ or Valence Band Offset from GaAs (eV)	VBO =-0.31	VBO = -0.092 (x=0.2) VBO = -0.368 (x=0.8)	$\chi = 4.07$	$\chi = 4.05$	$\chi = 4.0$
Dielectric constant	12.0	12.34 (x=0.2) 10.63 (x=0.8)	12.91	11.9	15.8
Bgn2Chi	0.5	0.5	0.5	0.5	0.5
Effective Conduction Band Density of States N_C (cm^{-3})	6.235×10^{17}	5.624×10^{17} (x=0.2) 1.5878×10^{19} (x=0.8)	4.352×10^{17}	ref. [55]	1.006×10^{19}

Effective Valence Band Density of States N_V (cm^{-3})	1.509×10^{17}	1.049×10^{19} (x=0.2) 1.498×10^{19} (x=0.8)	9.398×10^{18}	ref. [29]	4.989×10^{18}
Intrinsic Carrier Concentration n_i (cm^{-3})	1.072×10^{3}	8.65×10^{3} (x=0.2) 35.28 (x=0.8)	2.207×10^{6}	9.65×10^{9}	1.985×10^{13}

The `Bgn2Chi` parameter controls the fraction of the bandgap narrowing value that will appear as a change in electron affinity. A value of 0.5 means that if the band gap E_g is modified to $E_g - \Delta E_g$, the electron affinity will be modified as $\chi + 0.5\ \Delta E_g$.

A.2. Band Structure

A review paper by Vurgaftman [56] gives a thorough and up-to-date summary of band structure parameters for nearly the entire III-V material system, with the exception of band gap narrowing models and the effect of band gap narrowing on electron affinity. In general, the 'Piprek' MatPar models provided by Synopsys match the data in Vurgaftman, and these models are used where they are available. Currently in our Sentaurus models, band gap narrowing is only considered in GaAs and silicon.

'Fermi' and 'NoFermi' options

In order for simulations to be accurate in degenerately doped semiconductor regions, the '`Fermi`' option should be set in the `Physics{ }` section. This applies Fermi-Dirac statistics, rather than Maxwell-Boltzmann statistics. This raises a further complication though, since band gap-narrowing models that were developed using Maxwell-Boltzmann statistics would be incompatible with Fermi-Dirac simulations, and vice-versa. For this reason Sentaurus applies a

‘Fermi-Dirac correction’ by default to band gap narrowing models when ‘`Fermi`’ is enabled, under the assumption that the models were developed using Maxwell-Boltzmann statistics. In cases where the models were in fact developed using Fermi-Dirac statistics, the correction should be disabled using the ‘`NoFermi`’ option in each material section.

Much of the research on band gap narrowing since the 1990s recognizes this distinction, and so it appears that the ‘Jain-Roulston’, ‘Schenk’, and ‘Schubert’ band gap narrowing models are based on Fermi-Dirac statistics. For these models (and possibly others), the ‘`NoFermi`’ option should be used.

A.2.1. $Ga_{0.51}In_{0.49}P$

The ‘Piprek’ band gap model for GaInP gives a value of 1.96 eV at 300K, which is inconsistent with the ‘Schubert’ absorption model. A wide range of band gaps are possible for $Ga_{0.51}In_{0.49}P$ due to varying degrees of Cu:Pt ordering, where Ga and In atoms are sorted onto alternate group-III planes of the crystal lattice. A band gap value of 1.84 eV provides a good match to the Schubert absorption model, and also results in an intrinsic carrier density that agrees with the literature. Additionally, a value of ~1.84 eV is closer to the band gaps of existing commercial MJ solar cells. Researchers at NREL have published data on the Cu:Pt ordering dependence of the GaInP band gap; see the reference in the optical properties section below.

A.2.2. $Al_xGa_{1-x}As$

The bandgap of $Al_xGa_{1-x}As$ is direct for $x < 0.45$ and indirect otherwise. Band gap narrowing is not generally used for AlGaAs, and has sometimes been seen to cause problems with tunnel junction performance. The ‘Piprek’ band structure model is used, which is in close agreement with Vurgaftman.

A.2.3. GaAs

The ‘Piprek’ band structure model is used, which is in close agreement with Vurgaftman. Many different bandgap narrowing models are available in the literature, some of which show quite significant reduction in bandgap at high doping. In general the bandgap narrowing models with less drastic effect (‘Piprek’ and ‘Schubert’) have shown the best agreement with data. The ‘Schubert’ [57] model is chosen as the standard, as it is a fit to experimental data and has separate curves for *n*- and *p*-type material.

A.2.4. Silicon

The default Sentaurus values for the band gap of silicon are used, which agree well with values in the literature at 0 K and 300 K. The value of electron affinity χ is chosen to give 4.05 eV at 300 K. A simplified version of the band-gap narrowing model from Schenk is provided by Synopsys. In order to make it work properly in heterostructures, `Bgn2Chi` must be set to 0.5; this parameter is not defined in the stock Si.par file.

Careful measurements have shown the intrinsic carrier density n_i = 9.65x10^9 cm^{-3}. As recommended by Altermatt [29], the electron effective mass found by Green [55] is used, but the valence band density of states N_v is chosen to yield the required value of n_i.

A.2.5. Germanium

The ‘Default’ model for the germanium band gap is used. This model provides Sentaurus’ default values; no specific reference is available for this model, but the data roughly agrees with

Appendix F in Sze [24].

A.3. Mobility

A.3.1. III-V materials

Doping-dependent mobility models for all of the III-V materials are based on parameters from Sotoodeh [58], and are parameterized using the generic ‘Masetti’ model in Sentaurus which follows the formula

$$\mu_{dop} = \mu_{min1} \exp\left(\frac{-P_C}{N_A+N_D}\right) + \frac{\mu_{const}-\mu_{min2}}{1+\left(\frac{N_A+N_D}{C_r}\right)^{\alpha}} - \frac{\mu_1}{1+\left(\frac{C_s}{N_A+N_D}\right)^{\beta}}, \qquad \text{(A-1)}$$

where N_A and N_D are the acceptor and donor concentrations, respectively, and $\mu_{min1}, \mu_{const}, \mu_{min2}, \mu_1, P_C, C_r, C_s, \alpha$ and β are empirically determined fitting parameters.

All of the necessary parameters can be found in the Sotoodeh paper; the resulting mobilities are plotted in Figure 24. Like most other properties, mobility measurements in GaInP show much greater variability in data reported by different groups, likely due to differences in Cu:Pt

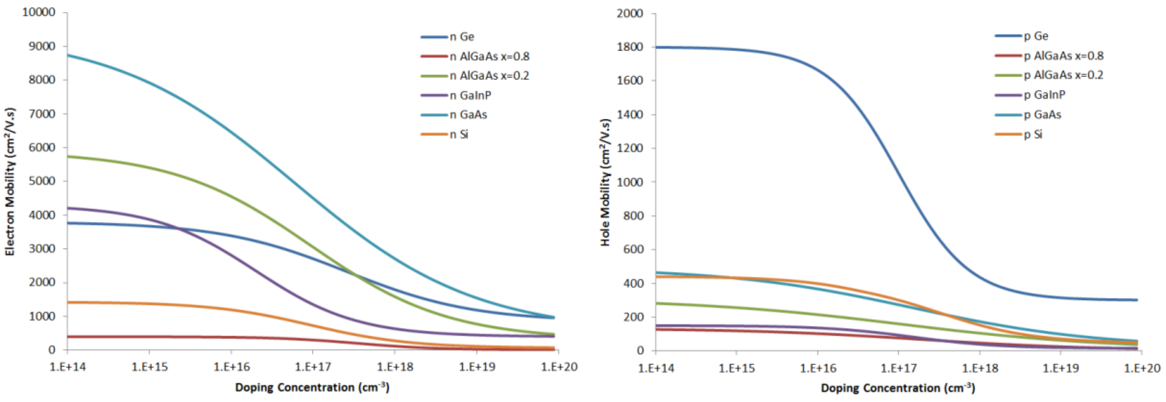

Figure 24: Electron (left) and hole (right) mobilities for various materials.

ordering of the group III atoms.

A.3.2. Silicon

For silicon, Sentaurus provides the ‘Phillips Unified Mobility Model’, which implements Klaassen’s silicon mobility model [59][60], including carrier-carrier interaction effects. This model is recommended in Altermatt’s review paper because it accounts for differences between the mobility of minority and majority carriers, and the mobility of minority carriers is particularly important due to the influence on diffusion length. No parameters are required for the model; it is selected by adding the following line to the silicon-specific Physics section in the Sentaurus command file:

```
Mobility ( PhuMob ( Phosphorus Klaassen ) )
```

Note that this model is not simply a function of acceptor and donor concentrations; it also takes into account the actual carrier concentrations.

A.3.3. Germanium

Mobility data for germanium is based on data from Palankovski [61], parameterised with the Arora model in Sentaurus.

A.4. Bulk Recombination

Three recombination processes are generally considered throughout the bulk material: radiative recombination, Shockley-Read-Hall recombination, and Auger recombination. For conditions near equilibrium, a minority-carrier lifetime is associated with each of these processes, as follows:

$$\tau_{n,Auger} = \frac{1}{A_n {N_A}^2}\,, \tag{A-2}$$

$$\tau_{n,SRH} = \frac{\tau_{n,max}}{1 + \left(\frac{N_A}{N_{ref}}\right)^{\gamma}}\,, \tag{A-3}$$

and

$$\tau_{n,Rad} = \frac{1}{B_{rad,n} N_A}\,, \tag{A-4}$$

where A_n, $\tau_{n,max}$, N_{ref}, and γ are empirically determined fitting coefficients. $B_{rad,n}$ is the radiative recombination coefficient, which can often be calculated analytically [22, p. 102].

The effective minority carrier lifetime is then given by

$$1/\tau_n = 1/\tau_{n,Auger} + 1/\tau_{n,SRH} + 1/\tau_{n,Rad}\,, \tag{A-5}$$

and the diffusion length is

$$L_n = \sqrt{q\mu_n\tau_n/kT}\,. \tag{A-6}$$

The above equations refer to minority electrons in *p*-type material; equivalent equations apply to minority holes in *n*-type material. Note that while these lifetimes indicate the dominant mechanism near equilibrium, a different process may dominate under illumination and/or bias. Also, some sources use a subscript '*n*' to denote *n*-type material, rather than electron carriers.

The parameters given in the following sections are intended to be used with Auger, radiative, and doping-dependent Shockley-Read-Hall processes enabled for all materials. Where γ is omitted, it can be assumed to be unity.

A.4.1. $Ga_{0.51}In_{0.49}P$

GaInP shows interesting changes in recombination lifetimes due to ordering and anisotropy of the crystal [62]. There is a limited amount of data available for the total bulk lifetime, and only for *p*-type and not-intentionally doped samples. The Auger coefficients below come from Strauss [63], and should never contribute significantly to recombination in this material. The parameters for Radiative and SRH processes are based on data from Haegel, and are not in agreement with Strauss' measurement.

Table 9: Recombination parameters for $Ga_{0.51}In_{0.49}$

	A (cm^{6}s^{-1})	B_{rad} (cm^{3}s^{-1})	τ_{max} (s)	N_{ref} (cm^{-3})
Electrons	$3x10^{-30}$	$2.4x10^{-10}$	$2x10^{-8}$	$1x10^{19}$
Holes	$3x10^{-30}$	$2.4x10^{-10}$	$2x10^{-8}$	$1x10^{19}$

Some additional data on minority carrier lifetime in GaInP can be found has been reported by King et. al. [64], showing higher lifetimes in some cases, as well as variations in lifetime as a function of ordering and doping.

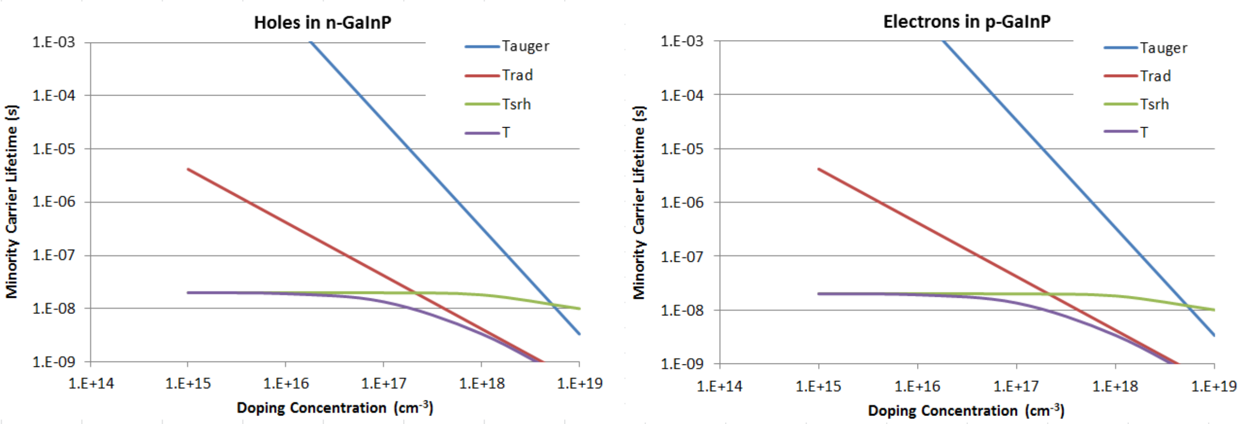

Figure 25: Hole (left) and Electron (right) lifetimes as a function of dopant concentration in GaInP.

A.4.2. $Al_xGa_{1-x}As$

The data below is from the 'Levinshtein' model, but the data in Levinshtein's book [65] is much less clear, and some dependence on mole fraction should probably be included. Since AlGaAs is not typically used in the active regions of solar cells, these inaccuracies should have a minimal effect on simulated device performance.

	A (cm^6s^{-1})	B_{rad} (cm^3s^{-1})	τ_{max} (s)	N_{ref} (cm^{-3})
Electrons	$1x10^{-30}$	$1x10^{-10}$	$1x10^{-9}$	$1x10^{16}$
Holes	$1x10^{-30}$	$1x10^{-10}$	$1x10^{-9}$	$1x10^{16}$

A.4.3. GaAs

For *p*-type GaAs, the situation is very clear – radiative recombination dominates at all doping levels [66]. There are few reliable measurements of the Auger coefficient for either *p*- or *n*-type material, but it has been shown that Auger recombination is insignificant in both *n*- and *p*-material, for doping levels up to $1x10^{19}$ cm^{-3}.

The case of *n*-type material is more complicated, though; radiative recombination is thought to be an important process in *n*-type material, at least in very high quality material, but the presence of photon recycling tends to negate its effect on device performance [67]. In lower quality material, the Shockley-Read-Hall mechanism seems to be dominant and shows a strong doping dependence at high doping concentrations.

The parameters given below are probably appropriate given that photon recycling is not accounted for in the model. In fact, the B_{rad} coefficient is larger (2×10^{-10} cm^3s^{-1}) but it would be inaccurate to set this value without also including photon recycling. The parameters for SRH recombination in *p*-type material have been arbitrarily chosen to ensure that Radiative recombination dominates at all doping levels.

	A (cm^6s^{-1})	B_{rad} (cm^3s^{-1})	τ_{max} (s)	N_{ref} (cm^{-3})	γ
Electrons	5×10^{-30}	1×10^{-10}	1×10^{-4}	1×10^{16}	1.0
Holes	5×10^{-30}	1×10^{-10}	2×10^{-8}	2×10^{18}	3.0

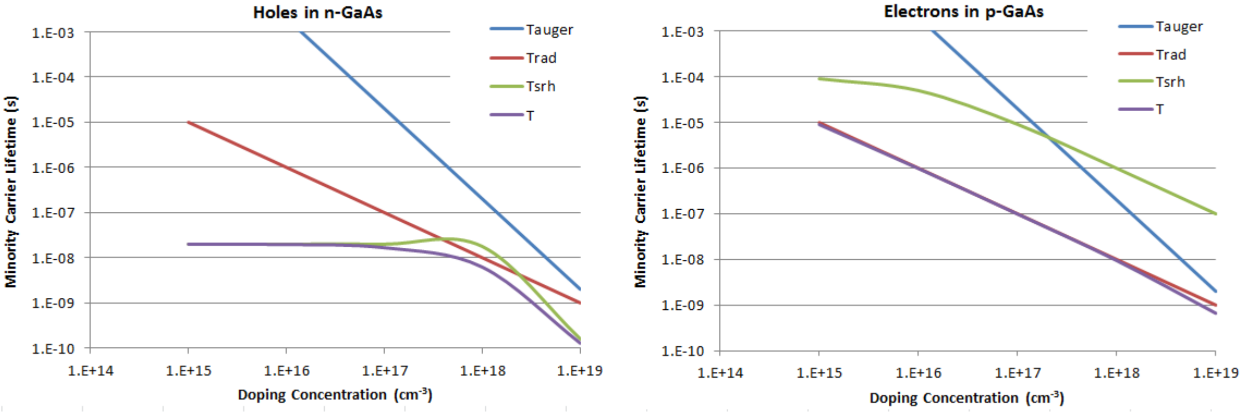

Figure 26: Hole (left) and electron (right) lifetimes as a function of dopant concentration in GaAs.

A.4.4. Silicon

For silicon, a more complex parameterization for the Auger coefficient is used:

$$A_n = A_{0,n}\left(1 + H_n \exp\frac{-n}{N_{0,n}}\right), \tag{A-7}$$

where $A_{0,n}$, H_n and $N_{0,n}$ are empirically determined fitting parameters and n is the density of electrons. A set of parameters is recommended by Altermatt, as shown below. The SRH parameters below are appropriate for modern float-zone silicon wafers; wafers grown by the

Czochralski method would have lower SRH lifetimes and a significant doping dependence.

	A_0 (cm^{6}s^{-1})	H	N_0 (cm^{-3})	B_{rad} (cm^{3}s^{-1})	τ_{max} (s)	N_{ref} (cm^{-3})
Electrons	7.91x10^{-32}	8	2.5x10^{17}	4.73x10^{-15}	1.5x10^{-3}	1x10^{18}
Holes	2.80x10^{-31}	8	2.5x10^{17}	4.73x10^{-15}	1.5x10^{-3}	1x10^{18}

A.4.5. Germanium

The recombination parameters given below for germanium are based on measurements by Spectrolab [68]. Auger and Radiative coefficients are set from values in the paper, and SRH parameters are adjusted to match the measured data points. The resulting diffusion lengths agree with experiments on Germanium solar cells reported by Friedman [69]. Levinshtein also reports some recombination parameters, but with much rounder numbers that lead to longer lifetimes.

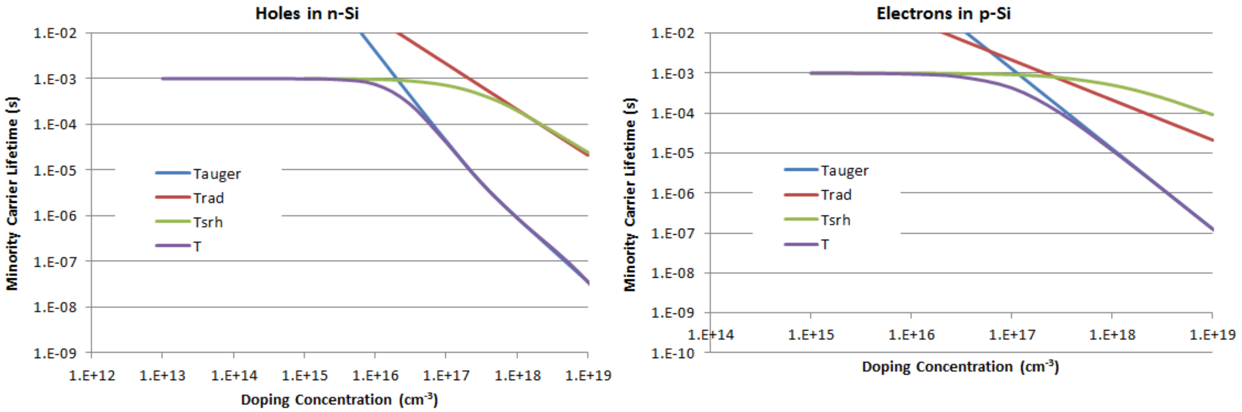

Figure 27: Hole (left) and electron (right) lifetimes as a function of dopant concentration in silicon.

	A (cm^{6}s^{-1})	B_{rad} (cm^{3}s^{-1})	τ_{max} (s)	N_{ref} (cm^{-3})
Electrons	2.8x10^{-31}	5.2x10^{-14}	2x10^{-5}	1x10^{17}
Holes	8x10^{-32}	5.2 x10^{-14}	4x10^{-5}	3x10^{16}

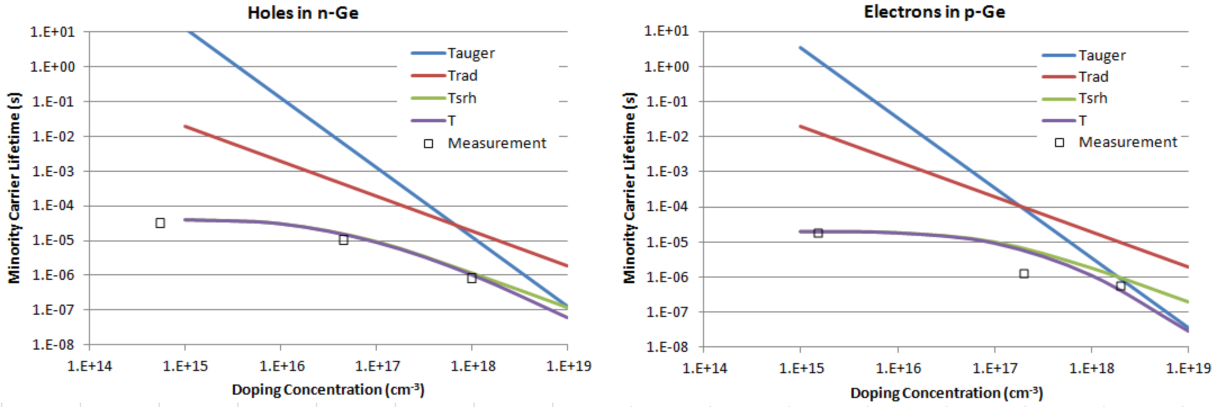

Figure 28: Hole (left) and electron (right) lifetimes as a function of dopant concentration in germanium.

A.5. Heterostructures and Surface Recombination

The options `HeteroInterface` and `ThermionicEmission` are enabled for the entire structure.

In a report on surface passivation in solar cells [70], Kurtz *et al*. refer to interfaces with surface recombination velocity (S) less than 10^4 cm/s as 'effectively ideal'. In general, surface/interface recombination can be omitted from the model at interfaces where S is less than this value. Kurtz gives the following table of interface recombination velocities reported in the literature; see the report for the original references.

GaAs Doping (cm^{-3})	**Barrier**	**S (cm/s)**
$\boldsymbol{n < 10^{16}}$	$Al_{0.3}Ga_{0.7}As$	18
$\boldsymbol{n < 10^{15}}$	$Ga_{0.5}In_{0.5}P$	<1.5
$\boldsymbol{n = 1\text{-}3 \times 10^{18}}$	$Ga_{0.5}In_{0.5}P$	1300
$\boldsymbol{n = 1.3 \times 10^{17}}$	$Al_{0.3}Ga_{0.7}As$	<12
$\boldsymbol{p = 5 \times 10^{15}}$	$Al_{0.5}Ga_{0.5}As$	300
$\boldsymbol{p = 3 \times 10^{16}}$	$Al_{0.5}Ga_{0.5}As$	350
$\boldsymbol{p = 1.7 \times 10^{17}}$	$Al_{0.5}Ga_{0.5}As$	500

$Ga_{0.51}In_{0.49}P$ Doping (cm^{-3})		
$p = 9x10^{16}$	$Al_{0.25}Ga_{0.25}In_{0.5}P$	140,000
$n < 10^{15}$	disordered $Ga_{0.5}In_{0.5}P$	<2
$n < 10^{15}$	$Al_{0.25}Ga_{0.25}In_{0.5}P$	7
$n < 10^{15}$	$Al_{0.5}In_{0.5}P$	85
$n < 10^{15}$	$Al_{0.5}Ga_{0.5}As$	180
$n < 10^{15}$	$Al_{0.85}Ga_{0.15}As$	>5000
Germanium Doping (cm^{-3})		
10^{18}	GaInP	1-2x10^{5} (from ref. [69])

A.6. Refractive Index and Optical Absorption

The wavelength-dependent complex index of refraction is tabulated for each material, described in the subsections below. The corresponding absorption coefficients are plotted here.

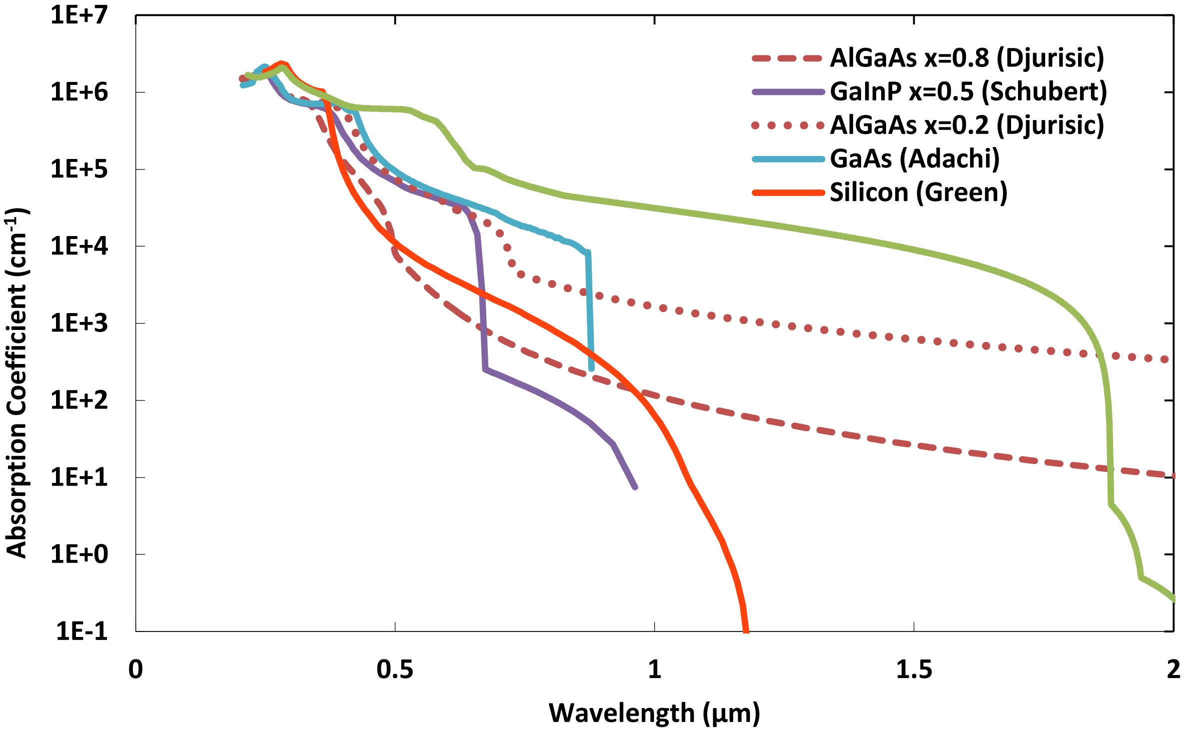

Figure 29: Optical absorption coefficients for each material.

A.6.1. $Ga_{0.51}In_{0.49}P$

Currently, the complex refractive index data for GaInP is from a paper by Schubert [71], and is only available for mole fraction x=0.51. These data are fairly rough. More recently, workers at NREL [72] have reported a more detailed set of measured data for three different values of the ordering parameter corresponding to different band gaps. These data may be more suitable for use in a multi-junction cell model.

A.6.2. $Al_xGa_{1-x}As$

The complex refractive index data for AlGaAs is from Djurisic [73], at 5% mole fraction intervals. Djurisic's paper actually gives a fit of an analytical expression, which could be calculated at any mole fraction.

A.6.3. GaAs

The optical absorption model file for GaAs was created by Alex Walker at University of Ottawa from Adachi [74]. This data set is widely referenced, but lacks resolution near the conduction band edge. It could be improved by incorporating doping-dependent data near the band edge from Casey [75] and the more recent data from Lundstrom [76].

A.6.4. Germanium

The complex refractive index data is from Palik [77].

A.6.5. Silicon

We use complex refractive index data from Green [78]. It is less noisy than the default

Sentaurus data in the area near the absorption edge. However, Green's data for extinction coefficient k has too few significant digits, so instead k has been calculated from the reported values of the absorption coefficient α.

References

[1] “Best Research-Cell Efficiencies,” *National Renewable Energy Laboratory Website*, 2012. [Online]. Available: http://www.nrel.gov/ncpv/images/efficiency_chart.jpg. [Accessed: 08-Jan-2013].

[2] S. D’Souza, J. Haysom, H. Anis, and K. Hinzer, “The Down-to-Earth Future of Si Substrate Multi-junction Concentrator Photovoltaics,” in *2011 IEEE Electrical Power and Energy Conference*, 2011, pp. 57–61.

[3] Z. S. Judkins, “A Market Analysis for High-Efficiency Multi-Junction Solar Cells Grown on SiGe,” MIT, 2007.

[4] A. Boucherif, “Elaboration de pseudosubstrats accordables en paramètre de maille à base de Silicium mésoporeux pour l’hétéroépitaxie,” Institut National des Sciences Appliquées de Lyon, 2010.

[5] N. P. Blanchard, A. Boucherif, P. Regreny, A. Danescu, H. Magoariec, J. Penuelas, V. Lysenko, J. Bluet, O. Marty, G. Guillot, and G. Grenet, “Engineering Pseudosubstrates with Porous Silicon Technology,” in *Semiconductor-On-Insulator Materials for Nanoelectronics Applications*, A. Nazarov, J.-P. Colinge, F. Balestra, J.-P. Raskin, F. Gamiz, and V. S. Lysenko, Eds. Berlin, Heidelberg: Springer Berlin Heidelberg, 2011, pp. 47–65.

[6] A. Boucherif, R. Arès, and V. Aimez, “APECS : Milestone 2 deliverables,” Sherberooke, 2012.

[7] S. Saravanan, Y. Hayashi, T. Soga, T. Jimbo, M. Umeno, N. Sato, and T. Yonehara, “Growth of GaAs epitaxial layers on Si substrate with porous Si intermediate layer by chemical beam epitaxy,” *J. Cryst. Growth* **237–239**, pp. 1450–1454, Apr. 2002.

[8] T. W. Kang, J. Y. Leem, and T. W. Kim, “Growth of GaAs epitaxial layers on porous silicon,” *Microelectronics Journal* **27**, pp. 423–436, 1996.

[9] T. W. Kang, Y. T. Oh, J. Y. Leem, and T. W. Kim, “Growth and optical studies of a GaAs epitaxial layer on porous Si (1 0 O) grown by molecular beam epitaxy,” *Journal of Materials Science Letters* **11**, pp. 392–395, 1992.

[10] S. A. Ringel, C. L. Andre, E. A. Fitzgerald, A. J. Pitera, and D. M. Wilt, “Multi-junction III-V photovoltaics on lattice-engineered Si substrates,” in *Photovoltaic Specialists Conference, 2005. Conference Record of the Thirty-First IEEE*, 2005, pp. 567–570.

[11] L. Canham, Ed., *Properties of Porous Silicon*. IEE INSPEC, 1997, p. 414.

[12] W. Theiβ, “Optical properties of porous silicon,” *Surf. Sci. Rep.* **29**, pp. 91–192, Aug. 1997.

[13] L. J. Gibson and M. F. Ashby, *Cellular Solids: Structure and Properties*, Second. Cambridge University Press, 1997, p. 510.

[14] V. Timoshenko, T. Dittrich, V. Lysenko, M. Lisachenko, and F. Koch, “Free charge carriers in mesoporous silicon,” *Phys. Rev. B* **64** (8), pp. 1–8, Aug. 2001.

[15] H. Arrand, “Optical Waveguides and Components Based on Porous Silicon,” University of Nottingham, 1997.

[16] Y. B. Bolkhovityanov and O. P. Pchelyakov, “GaAs epitaxy on Si Substrates: Modern Status of Research and Engineering,” *Physics - Uspekhi* **51** (5), pp. 437–456, 2008.

[17] C. W. Pei, B. Turk, W. I. Wang, and T. S. Kuan, “Mechanism of the reduction of dislocation density in epilayers grown on compliant substrates,” *J. Appl. Phys.* **90** (12), p. 5959, 2001.

[18] P. Gay, P. B. Hirsch, and A. Kelly, “The Estimation of Dislocation Densities in Metals from X-Ray Data,” *Acta Metallurg.* **1**, pp. 315–319, 1953.

[19] R. T. Blunt, S. Clark, and D. J. Stirland, “Dislocation Density and Sheet Resistance Variations across Semi-Insulationg GaAs Wafers,” *IEEE T. Microw. Theory.* **MTT-30** (7), pp. 943–949, 1982.

[20] C. L. Andre, A. Khan, M. Gonzalez, M. K. Hudait, E. A. Fitzgerald, J. A. Carlin, M. T. Currie, C. W. Leitz, T. A. Langdo, E. B. Clark, D. M. Wilt, and S. A. Ringel, “Impact of Threading Dislocations on both n/p and p/n Single Junction GaAs Cells Grown on Ge / SiGe / Si Substrates,” in *Conference Record of the Twenty-ninth IEEE Photovoltaic Specialists Conference*, 2002, (001), pp. 1043–1046.

[21] J. E. Ayers, “The measurement of threading dislocation densities in semiconductor crystals by X-ray diffraction,” *J. Cryst. Growth* **135** (1)–(2), pp. 71–77, Jan. 1994.

[22] J. Nelson, *Physics of Solar Cells*. London: Imperial College Press, 2003, p. 363.

[23] B. G. Streetman, *Solid State Electronics Devices*, 4th ed. Upper Saddle River, NJ: Prentice-Hall, 1995, p. 462.

[24] S. M. Sze and K. N. Kwok, *Physics of Semiconductor Devices*, 3rd ed. Hoboken, NJ: Wiley-Interscience, 2007, p. 832.

[25] J. F. Wheeldon, C. E. Valdivia, A. W. Walker, G. Kolhatkar, A. Jaouad, A. Turala, B. Riel, D. Masson, N. Puetz, S. Fafard, R. Ares, V. Aimez, T. J. Hall, and K. Hinzer, “Performance comparison of AlGaAs , GaAs and InGaP tunnel junctions for concentrated multijunction solar cells,” *Prog. Photovolt.: Res. Appl.* **19** (4), pp. 442–452, 2010.

[26] T. Yu, M. M. R. Howlader, F. Zhang, and M. Bakr, “Nanobonding for Multi-Junction Solar Cells at Room Temperature,” *ECS Transactions* **35** (2), pp. 3–10, 2011.

[27] “Sentaurus Device User Guide ver. F-2011.09,” 2011.

[28] “Sentaurus Workbench User Guide, ver. F-2011.09,” 2011.

[29] P. P. Altermatt, “Models for numerical device simulations of crystalline silicon solar cells—a review,” *J. Comput. Electron.* **10** (3), pp. 314–330, Jul. 2011.

[30] W. Fichtner, D. J. Rose, and R. E. Bank, “Semiconductor device simulation,” *IEEE T. Electron. Dev.* **30** (9), pp. 1018–1030, Sep. 1983.

[31] R. E. Bank, D. J. Rose, and W. Fichtner, “Numerical Methods for Semiconductor Device Simulation,” *IEEE T. Electron. Dev.* **ED-30** (9), pp. 1031–1041, 1983.

[32] A. F. Franz, G. A. Franz, S. Selberherr, C. Ringhofer, and P. Markowich, “Finite Boxes-A Generalization of the Finite-Difference : Method Suitable for Semiconductor Device Simulation,” *IEEE T. Electron. Dev.* **ED-30** (9), pp. 1070–1082, 1983.

[33] C. M. Wu and E. S. Yang, “Carrier Transport across Heterojunction Interfaces,” *Solid-State Electron.* **22**, pp. 241–248, 1979.

[34] K. Horio and H. Yanai, “Numerical Modeling of Heterojunctions Including the Thermionic Emission Mechanism at the Heteroj unction Interface,” *IEEE T. Electron. Dev.* **37** (4), pp. 1093–1098, 1990.

[35] “ASTM G173-03 (2008) Standard Tables for Reference Solar Spectral Irradiances: Direct Normal and Hemispherical on 37 degree Tilted Surface,” 2008.

[36] M. Wilkins, “Parameters for Modeling Multi-junction Solar Cells in Sentaurus,” Ottawa, 2012.

[37] M. A. Green, K. Emery, Y. Hishikawa, and W. Warta, “Solar cell efficiency tables (version 36),” *Prog. Photovolt.: Res. Appl.* **18** (5), pp. 346–352, Jun. 2010.

[38] M. A. Green, K. Emery, Y. Hishikawa, W. Warta, and E. D. Dunlop, “Solar cell efficiency tables (version 39),” *Prog. Photovolt.: Res. Appl.*, pp. 12–20, 2012.

[39] G. Létay, “Modellierung von III-V Solarzellen,” Ph. D Dissertation, Fakultät für Physik, Universität Konstanz, 2003.

[40] H. Looyenga, “Dielectric constants of heterogeneous mixtures,” *Physica* **31** (3), pp. 401–406, Mar. 1965.

[41] A. J. Simons, T. I. Cox, M. J. Uren, and P. D. J. Calcott, "The electrical properties of porous silicon produced from n+ silicon substrates," *Thin Solid Films* **255** (1)–(2), pp. 12–15, Jan. 1995.

[42] L. A. Balagurov, D. G. Yarkin, and E. A. Petrova, "Electronic transport in porous silicon of low porosity made on a p + substrate," *Mater. Sci. Eng., B* **69–70**, pp. 127 – 131, 2000.

[43] M. Yamaguchi and C. Amano, "Efficiency calculations of thin-film GaAs solar cells on Si substrates," *J. Appl. Phys.* **58** (9), p. 3601, 1985.

[44] D. L. Dexter and F. Seitz, "Effects of Dislocations on Mobilities in Semiconductors," *Phys. Rev.* **86** (6), pp. 964–965, 1952.

[45] A. Boucherif, N. P. Blanchard, P. Regreny, O. Marty, G. Guillot, G. Grenet, and V. Lysenko, "Tensile strain engineering of Si thin films using porous Si substrates," *Thin Solid Films* **518** (9), pp. 2466–2469, Feb. 2010.

[46] M. W. Wanlass, S. P. Ahrenkiel, D. S. Albin, J. J. Carapella, A. Duda, K. Emery, J. F. Geisz, K. Jones, S. Kurtz, T. Moriarty, and M. J. Romero, "GaInP / GaAs / GaInAs Monolithic Tandem Cells for High-Performance Solar Concentrators," in *International Conference on Solar Concentrators for the Generation of Electricity or Hydrogen*, 2005, (May).

[47] S. Roensch, R. Hoheisel, F. Dimroth, and A. W. Bett, "Subcell I-V characteristic analysis of GaInP/GaInAs/Ge solar cells using electroluminescence measurements," *Appl. Phys. Lett.* **98** (25), p. 251113, 2011.

[48] D. J. Friedman, S. R. Kurtz, K. A. Bertness, A. E. Kibbler, C. Kramer, and J. M. Olson, "30.2% Efficient GaInP/GaAs Monolithic Two-terminal Tandem Concentrator Cell," *Prog. Photovolt.: Res. Appl.* **3**, pp. 47–50, 1995.

[49] M. Wolf, "Drift Fields in Photovoltaic Solar Energy," *Proceeding of the IEEE* **51** (5), pp. 674–693, 1963.

[50] "Sunpower Inc." [Online]. Available: us.sunpower.com. [Accessed: 26-Jan-2013].

[51] "29.5% NeXt Triple Junction (XTJ) Solar Cells." Spectrolab, 2012.

[52] M. A. Green, K. Emery, Y. Hishikawa, and W. Warta, "Solar Cell Efficiency Tables (Version 33)," *Prog. Photovolt.: Res. Appl.* **17**, pp. 85–94, 2009.

[53] C. W. Pei, J. B. Héroux, J. Sweet, W. I. Wang, J. Chen, and M. F. Chang, "High quality GaAs grown on Si-on-insulator compliant substrates," *Journal of Vacuum Science & Technology B* **20** (3), pp. 1196–1199, 2002.

[54] Y. Takano, M. Hisaka, N. Fujii, K. Suzuki, K. Kuwahara, and S. Fuke, "Reduction of threading dislocations by InGaAs interlayer in GaAs layers grown on Si substrates," *Appl. Phys. Lett.* **73** (20), p. 2917, 1998.

[55] M. A. Green, "Intrinsic concentration, effective densities of states, and effective mass in silicon," *J. Appl. Phys.* **67** (6), pp. 2944–2954, 1990.

[56] I. Vurgaftman, J. R. Meyer, and L. R. Ram-Mohan, "Band parameters for III–V compound semiconductors and their alloys," *J. Appl. Phys.* **89** (11), p. 5815, 2001.

[57] E. F. Schubert, *Physical Foundations of Solid-State Devices*. Rensselaer Polytechnic Institute, 2007.

[58] M. Sotoodeh, A. H. Khalid, and A. A. Rezazadeh, "Empirical low-field mobility model for III–V compounds applicable in device simulation codes," *J. Appl. Phys.* **87** (6), p. 2890, 2000.

[59] D. B. M. Klaassen, "A Unified Mobility Model for Device Simulation -- I . Model Equations and Concentration Dependence," *Solid-State Electron.* **35** (7), pp. 953–959, 1992.

[60] D. B. M. Klaassen, "A Unified Mobility Model for Device Simulation -- II . Temperature Dependence of Carrier Mobility and Lifetime," *Solid-State Electron.* **35** (7), pp. 961–967, 1992.

[61] V. Palankovski and R. Quay, *Analysis and Simulation of Heterosturcture Devices*. Vienna: Springer-Verlag, 2004, p. 289.

[62] N. M. Haegel, S. E. Williams, C. L. Frenzen, and C. Scandrett, “Minority carrier lifetime variations associated with misfit dislocation networks in heteroepitaxial GaInP,” *Semicond. Sci. Technol.* **25** (5), p. 055017, May 2010.

[63] U. Strauss, W. W. Rühle, H. J. Queisser, K. Nakano, and a. Ishibashi, “Band-to-band recombination in Ga0.5In0.5P,” *J. Appl. Phys.* **75** (12), p. 8204, 1994.

[64] R. R. King, C. M. Fetrer, P. C. Colter, K. M. Edmondson, H. E. James, H. L. Cotal, H. Yoon, A. P. Stavrides, G. Kinsey, D. D. Krut, and N. H. Karam, “High-Efficiency Space and Terrestrial Multijunction Solar Cells Through Bandgap Control in Cell Structures,” in *Photovoltaic Specialists Conference, 2002. Conference Record of the Twenty-Ninth IEEE*, 2002, pp. 776–781.

[65] Y. A. Goldberg, “Aluminum Gallium Arsenide (AlxGa1-xAs),” in *Handbook Series on Semiconductor Parameters, vol. 2*, M. Levinshtein, S. Rumyantev, and M. Shur, Eds. World Scientific, 1999, p. 205.

[66] M. S. Lundstrom, M. E. Klausmeier-Brown, M. R. Melloch, R. K. Ahrenkiel, and B. M. Keyes, “Device-related Material Properties of Heavily Doped Gallium Arsenide,” *Solid-State Electron.* **33** (6), pp. 693–704, 1990.

[67] G. B. Lush, H. F. MacMillan, B. M. Keyes, D. H. Levi, M. R. Melloch, R. K. Ahrenkiel, and M. S. Lundstrom, “A study of minority carrier lifetime versus doping concentration in n-type GaAs grown by metalorganic chemical vapor deposition,” *J. Appl. Phys.* **72** (4), p. 1436, 1992.

[68] H. Yoon, K. M. Edmondson, G. S. Kinsey, R. R. King, P. Hebert, R. K. Ahrenkiel, B. T. Cavicchi, and N. H. Karam, “Minority Carrier Lifetime and Radiation Damage Coefficients of Germanium,” *Conference Record of the Thirty-first IEEE Photovoltaic Specialists Conference*, pp. 842–845, 2005.

[69] D. J. Friedman and J. M. Olson, “Analysis of Ge junctions for GaInP/GaAs/Ge three-junction solar cells,” *Prog. Photovolt.: Res. Appl.* **9** (3), pp. 179–189, May 2001.

[70] S. R. Kurtz, J. M. Olson, D. J. Friedman, J. F. Geisz, and A. E. Kibbler, “Passivation of Interfaces in High-Efficiency Photovoltaic Devices,” in *Materials Research Society Spring Meeting*, 1999, (May).

[71] M. Schubert, V. Gottschalch, C. M. Herzinger, H. Yao, P. G. Snyder, and J. A. Woollam, “Optical constants of GaxIn1−xP lattice matched to GaAs,” *J. Appl. Phys.* **77** (7), p. 3416, 1995.

[72] D. H. Levi, “Effects of ordering on the optical properties of GaInP,” *Proceedings of SPIE* **5530**, pp. 326–337, 2004.

[73] A. B. Djurisic, A. D. Rakic, P. C. K. Kwok, E. H. Li, M. L. Majewski, and J. M. Elazar, “Modeling the Optical Constants of Al(x)Ga(1-x)As Alloys,” *J. Appl. Phys.* **86** (1), pp. 445–451, Nov. 1999.

[74] S. Adachi, *Optical Constants of Crystalline and Amorphous Semiconductors*. Springer, 1999, p. 714.

[75] H. C. Casey, D. D. Sell, and K. W. Wecht, “Concentration dependence of the absorption coefficient for n− and p−type GaAs between 1.3 and 1.6 eV,” *J. Appl. Phys.* **46** (1), p. 250, 1975.

[76] M. S. Lundstrom, M. R. Melloch, G. B. Lush, G. J. O’Bradovich, and M. P. Young, “New III-V Cell Design Approaches for Very High Efficiency: Annual Subcontract Report 1990 - 1991,” 1991.

[77] E. D. Palik, *Handbook of Optical Constants of Solids*. 1998, p. 1096.

[78] M. A. Green and M. J. Keevers, “Optical Properties of Intrinsic Silicon at 300 K,” *Prog. Photovolt.: Res. Appl.* **3** (3), pp. 189–192, 1995.